

Fibrous-Structured Freestanding Electrodes for Oxygen Electrocatalysis

Shan Jiang, Jingliang Li, Jian Fang, and Xungai Wang*

Electrocatalysts used for oxygen reduction and oxygen evolution reactions are critical materials in many renewable-energy devices, such as rechargeable metal–air batteries, regenerative fuel cells, and water-splitting systems. Compared with conventional electrodes made from catalyst powders, oxygen electrodes with a freestanding architecture are highly desirable because of their binder-free fabrication and effective elimination of catalyst agglomeration. Among all freestanding electrode structures that have been investigated so far, fibrous materials exhibit many unique advantages, such as a wide range of available fibers, low material and material-processing costs, large specific surface area, highly porous structure, and simplicity of fiber functionalization. Recent advances in the use of fibrous structures for freestanding electrocatalytic oxygen electrodes are summarized, including electrospun nanofibers, bacterial cellulose, cellulose fibrous structures, carbon clothes/papers, metal nanowires, and metal meshes. After detailed discussion of common techniques for oxygen electrode evaluation, freestanding electrode fabrication, and their electrocatalytic performance, current challenges and future prospects are also presented for future development.

1. Introduction

With increasing demands for clean and sustainable energy sources, the development of low-cost and efficient renewable energy technologies has received enormous attention from both industrial and academic sections in recent years. Among all renewable energy conversion and storage systems currently under investigation, metal–air batteries and fuel cells have stood out as the most promising candidates owing to their high energy density and environmentally friendly energy conversion process.^[1] They generate electricity through the redox reactions between a fuel anode (H_2 for fuel cells; Zn, Li, Na, etc., for metal–air batteries) and an air cathode.

For the similarly structured air cathode in these energy devices, there are two fundamental electrochemical processes

on electrode surface: oxygen reduction reaction (ORR) for converting O_2 to O^{2-} and oxygen evolution reaction (OER) in the reverse direction. Theoretically, the equilibrium potential should be 1.23 V versus reversible hydrogen electrode (RHE). However, their complex electron pathway and sluggish kinetics always cause the actual potential value to deviate from the ideal one, leading to a high overpotential.^[2] This has become a serious obstacle impeding the wide spread application of these technologies. Therefore, in order to improve electrode efficiency for practical use, it is critical to exploit highly efficient oxygen electrocatalysts for accelerating the reaction rates.

Although ORR and OER are a reverse reaction couple, in reality a good ORR electrocatalyst does not guarantee ideal OER performance under the same conditions. In the past few decades, a wide range of functional materials have been

developed for ORR and OER catalysis with promising electrocatalytic performance. **Table 1** summarizes some typical oxygen electrocatalysts that have been investigated so far.^[3–9]

Although great successes have been achieved in the development of active oxygen electrocatalysts, almost all currently used catalysts still suffer from their powdery form. During oxygen electrode fabrication, electrocatalyst powders are normally mixed with carbon black, organic binder, and solvent to form a catalyst paste and then applied onto conductive current collector to form final electrode after oven drying. The multistep electrode fabrication does not only involve tedious processes, but also has many drawbacks. The agglomeration of catalyst powders during electrode fabrication can considerably reduce the surface area of the electrode. The use of nonconductive polymeric binder deteriorates the electrical conductivity of electrode and causes blockage of active catalytic sites, both leading to reduced electrocatalytic performance. In addition, harsh electrochemical condition during charge–discharge cycles can decompose the organic components in the catalytic electrode and endanger its structural integrity. Finally, the use of organic solvent for paste preparation can pose safety hazards, with serious environmental and health concerns.^[10] In this regard, fabricating freestanding electrocatalytic oxygen electrode from easily available low-cost material to avoid the pre-preparation of electrocatalyst powders and the use of any organic binder and solvent, while at the same time, to achieve high catalytic activity and durability is of practical

S. Jiang, Prof. J. L. Li, Dr. J. Fang, Prof. X. G. Wang
Institute for Frontier Materials
Deakin University
Geelong, VIC 3216, Australia
E-mail: xungai.wang@deakin.edu.au

Dr. J. Fang, Prof. X. G. Wang
ARC Centre of Excellence for Electromaterials Science (ACES)
Geelong, Victoria 3216, Australia

 The ORCID identification number(s) for the author(s) of this article can be found under <https://doi.org/10.1002/smll.201903760>.

DOI: 10.1002/smll.201903760

Table 1. A summary of common ORR and OER electrocatalysts.

Reaction	Electrocatalyst type	Material
ORR	Precious metals/alloys	Pt, PtPd
	Non-noble metal materials	Transition metal and nitrogen complex supported on carbon (M-N _x /C); Metal carbides/nitrides.
	Metal-free catalysts	Heteroatom single/double doped carbon nanomaterials (carbon nanotubes, graphene, carbon black, carbon nanofibers, and carbon nitrides).
OER	Metal oxides	Precious metal oxides (RuO ₂ , IrO ₂); Transition metal oxides (e.g., Co ₃ O ₄ , Mn ₂ O ₃); Mixed oxides (e.g., LaNiO ₃ , NiCo ₂ O ₄).
	Other metal containing species	Metal chalcogenides/nitrides/phosphides; Organometallics.
	Nonmetal compounds	Heteroatom doped carbon nanomaterials (carbon nanotubes, graphene and carbon nitrides).

importance to the future development of metal–air batteries and fuel cells.^[11]

Typically, the fabrication strategy for such binder-free structures can be divided into two categories: 1) Template-free fabrication, during which catalytic materials or their precursors are incorporated with organic sources to form a freestanding structure. Alternatively, organic freestanding structure can be used as a substrate for supporting functional materials or their precursors. A high temperature pyrolysis or calcination treatment is often required in both approaches to obtain electroactive free-standing electrodes. For example, electrospinning is a popular approach in preparing freestanding nanofibrous structures. A carbonization process can turn polymeric nanofiber web to conductive carbon nanofiber network with controllable fiber diameter and porous structure. Different inorganic active materials or heteroatom dopants can be introduced into fiber matrix during electrospinning. Similarly, graphene oxide nanosheets have many surface functional groups and can interact with different active materials to form composite structures and be turned to graphene-based freestanding electrocatalytic electrodes through thermal or chemical reduction. 2) Template-supported fabrication, which involves the deposition of catalytic materials on a pre-existing substrate, including carbon substrates, metal substrates, and some other conductive freestanding structures. The electrocatalytically active materials can be deposited or in situ grown on these substrates to form a composite structure. The commonly used carbon substrates include carbon fiber papers (CFP) and carbon clothes (CC). In terms of metal substrates, there are metal foams (e.g., Ni and Cu foams), metal meshes (e.g., Ti and stainless steel mesh), metal plates/foils (e.g., Ti plate, Mo, and Cu foils), etc.^[12–14] Notably, various metal compounds in different morphologies (nanoparticles/nanorods/nanosheets) have been successfully produced on Ni foams for water splitting electrolyzer.^[15–17] Benefited from their excellent mechanical property and flexibility, graphene nanosheets and carbon nanotubes have been coupled with nanocatalysts to form freestanding electrodes via different approaches. In particular,



Shan Jiang received her B.S. (2013) and M.S. (2016) degrees both in textile materials design from Wuhan Textile University (China). She is currently a Ph.D. student in the Institute for Frontier Materials at Deakin University (Australia). Her research focuses on the design and fabrication of high-performance electrocatalysts from biomass materials for applications such as oxygen reduction, oxygen evolution, and hydrogen evolution.



Jian Fang received his Ph.D. degree in materials engineering from Deakin University in 2009. He worked as a senior research fellow in the Institute for Frontier Materials (IFM) at Deakin University. In 2019, he took a full professor position in the College of Textile and Clothing Engineering at Soochow University in China.

His research focuses on functional fibrous materials for energy storage and harvesting device, biosensing, and environment protection applications.



Xungai Wang is the Pro Vice-Chancellor (Future Fibres) at Deakin University, Australia. He initiated the fibre and textile research at Deakin 20 years ago and has led the rapid expansion of research in the area. He also serves as the Director of the ARC Research Hub for Future Fibres. Prof. Wang holds a Ph.D. in fibre science and

technology and a Graduate Diploma in Higher Education from the University of New South Wales, Sydney. In 2006, he was named Alfred Deakin Professor, the highest honour that Deakin University can bestow on a member of staff. He served as President of the Fiber Society in 2015.

graphene aerogels, as a 3D graphene structure with high surface area and superior porous structure for ion transfer, have been extensively studied as freestanding carbon electrode.^[18–20]

It should be noted that among all above-mentioned free-standing structures, fibrous materials have exhibited many unique advantages during electrode fabrication and electrocatalytic application.^[21] Fibers normally refer to these flexible

1D materials with an aspect ratio greater than 1000. Individual fibers can be processed into different fiber assemblies and more complex fibrous structures, such as 1D yarns, 2D fibrous webs, and 3D fibrous structures.

Except for high length-to-diameter ratio, fibrous materials have many other advantages in using as oxygen electrocatalysts: 1) There are a wide range of fibrous materials with different physical dimensions and chemical structures for selection. 2) The advances in textile engineering and fiber science have enabled us to process fibrous materials into different free-standing structures with controllable porosity and dimension. 3) Compared with 0D powders, fibers are 1D materials that can efficiently overcome the issue of material agglomeration by forming porous structures, which also benefits the mass diffusion and ion transportation during electrochemical processes. On the other hand, 2D materials can also be processed to free-standing membrane structures. However, compared with 1D fibers, more costly, time-consuming or energy intensive approaches (such as templating method, thermal expansion, and freeze-drying) have to be used with 2D materials to form highly porous membrane structures with large number of active sites. 4) Fibrous materials are being widely used in many different industrial applications and largely available, which provide more competitive opportunities in developing low-cost electrode for energy devices. 5) Conductive fibers, such carbon fibers, are commercially produced on a large scale. The existing knowledge of fiber production and application can facilitate the development of fibrous freestanding electrodes.

In recent years, growing research efforts have been devoted to fabricating freestanding electrodes for various energy devices, with many excellent research and review papers published.^[11–14,22] However, the use of fibrous materials in freestanding electrodes, especially oxygen electrodes, has not yet been systematically summarized. In this article, we provide a comprehensive overview of the state-of-the-art research on fibrous-structured freestanding electrodes for oxygen electrocatalysis. The basic oxygen electrochemistry and evaluation criteria will be first introduced, followed by detailed discussion on the fabrication and electrocatalytic performance of various types of freestanding oxygen electrodes obtained from different fibrous sources (electrospun nanofibers, bacterial cellulose, cellulose fibrous structures, CFP, CC, metal nanowires, and metal meshes, etc.). Finally, the challenges and prospects are discussed for future development in the field.

2. Oxygen Electrochemistry

2.1. Fundamental Electrochemistry of Oxygen Electrode

2.1.1. ORR

Catalytic reaction on an electrode surface can be primarily divided into three steps: reactant adsorption, redox reactions on catalyst surface (charge transfer, proton transfer, bond breaking, and formation), and resultant desorption. The reason why a catalyst can adjust the reaction rate is attributed to certain interactions between the catalyst and the reactant, which result in the change of reaction route, thus decreasing the activation energy

Table 2. Two possible ORR mechanisms in an alkali solution.^[24]

ORR pathway	Mechanism	Reaction steps
4e [−]	Dissociative	$O_2 + 2* \rightarrow 2O_{(ad)}^{a)}$
		$2O_{(ad)} + 2e^- + 2H_2O \rightarrow 2OH_{(ad)} + 2OH^-$
		$2OH_{(ad)} + 2e^- \rightarrow 2OH^- + 2*$
	Associative	$O_2 + * \rightarrow O_{2(ad)}$
		$O_{2(ad)} + H_2O + e^- \rightarrow OOH_{(ad)} + OH^-$
		$OOH_{(ad)} + e^- \rightarrow O_{(ad)} + OH^-$
		$O_{(ad)} + e^- + H_2O \rightarrow OH_{(ad)} + OH^-$
2e [−]	Associative	$OH_{(ad)} + e^- \rightarrow OH^- + *$
		$O_2 + * \rightarrow O_{2(ad)}$
		$O_{2(ad)} + H_2O + e^- \rightarrow OOH_{(ad)} + OH^-$
		$OOH_{(ad)} + e^- \rightarrow OOH^- + *$

^{a)}Where * denotes an active site on the electrode surface.

and overpotentials.^[23] According to the initial O₂ adsorption pattern during oxygen reduction reaction, there are two possible catalytic mechanisms: dissociative mode and associative mode.

Table 2 shows the specific ORR reaction steps in an alkali solution (similar equations can also be determined in acid solutions). In the dissociative mode, O₂ is adsorbed with O–O bond breaking, leading to two adsorbed O_(ad), while oxygen molecule is adsorbed onto electrode surface by forming O_{2(ad)} in the associative mode. The 4-electron (4e[−]) ORR reaction turning O₂ to OH[−] may happen in both modes, which has low overpotentials and is highly preferred in air cathode operation. By contrary, 2-electron (2e[−]) ORR pathway with peroxide generation only exists in the associative mode, which is usually used in industrial H₂O₂ production.

Whether an ORR reaction follows the dissociative or the associative pathway depends on the oxygen adsorption mode and the oxygen dissociation energy barrier on the surface of a given catalyst. For example, it has been found that ORR processes on carbonaceous materials are more likely to take the 2e[−] pathway with very high dissociation energy barriers.^[27] On the contrary, the dissociative mode dominates the ORR process on most metal surfaces with strong O₂ adsorption energy. However, not all metals can exhibit good ORR activity, as it is closely related to the balance between the oxygen adsorption and intermediates release. For understanding ORR performance of a variety of close-packed metal surfaces, a volcano plot has been constructed to reveal the relationship between theoretical ORR activity and oxygen binding energy (ΔE_O), as shown in **Figure 1a**. For non-precious metals like Au that can strongly bind oxygen, their ORR activity is limited by proton–electron transfer to O(ad) or OH(ad). On the other hand, for metals like Mo that only weakly bind oxygen, the adsorbed oxygen is easy to escape, decreasing the possibility of the subsequent reactions. It can also be found that precious metal platinum (Pt) sits near the top of the plot, which has been one of the best performed ORR electrocatalysts so far, even though with a moderate level of oxygen binding strength.

2.1.2. OER

In the case of oxygen evolution reaction from H₂O to O₂, possible reaction pathways have also been proposed. Equations (1)–(6)

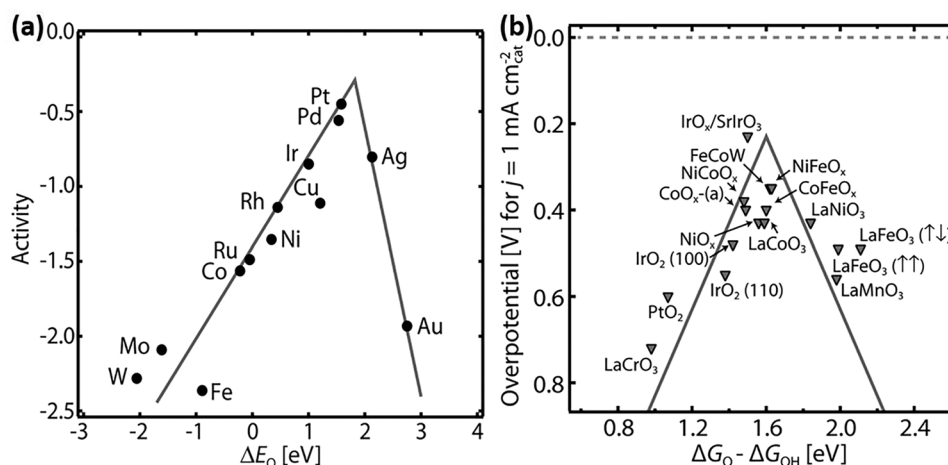
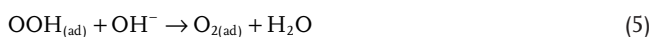
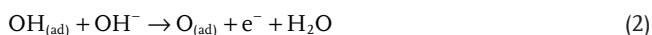


Figure 1. a) ORR volcano plot for metals. Reproduced with permission.^[25] Copyright 2004, American Chemical Society. b) OER volcano plot for metal oxides. Reproduced with permission.^[26] Copyright 2017, The American Association for the Advancement of Science.

show the widely accepted electron transfer steps in an alkali condition. Generally, it is almost a reverse process of the associative $4e^-$ pathway of ORR, with the same intermediates, such as $\text{OH}_{(\text{ad})}$ and $\text{O}_{(\text{ad})}$. But there is still a controversy on the generation of oxygen from $\text{O}_{(\text{ad})}$. One theory prefers the direct combination of $2\text{O}_{(\text{ad})}$ to produce O_2 (Equation (3)), and the other one advocates the formation of $\text{OOH}_{(\text{ad})}$ (Equations (4)–(6)) which subsequently decomposes to O_2 .^[3]



Similarly, a volcano plot has also been constructed to visualize the relationship between the intermediates (OH_{ad} , O_{ad}) adsorption free energy ($\Delta G_O - \Delta G_{OH}$) on a wide variety of metal oxide surfaces and the OER activity (experimental overpotentials at 1 mA cm^{-2}), as shown in Figure 1b. Experimental overpotentials at 1 mA cm^{-2} overlay well on the theoretical overpotential volcano when plotted against this simple descriptor. Although IrO_2 has been experimentally demonstrated as a good OER catalyst, it is still far from the most ideal OER catalyst in terms of activity and stability. It can be seen that energy value of $\Delta G_O - \Delta G_{OH}$ of IrO_2 is relatively low. Recently, thin films of $\text{IrO}_x/\text{SrIrO}_3$ were reported with extremely high OER activity in acid along with promising stability, which stands near the top of the volcano plot with moderate energy value of $\Delta G_O - \Delta G_{OH}$.^[26]

Therefore, it can be understood that there is a fundamental reason why a good ORR catalyst is usually not suitable for OER, which is correlated to the difference in the adsorption strengths to intermediates. Specifically, for a given electrode with good ORR performance, its oxygen binding energy is strong, and

the adhesion to $\text{OH}_{(\text{ad})}$ and $\text{O}_{(\text{ad})}$ should be relatively weak for yielding a high number of active sites. However, the same conditions are unfavorable for an OER process, as it is hard to adsorb the reactants onto electrode surface, therefore difficult for the generated gas O_2 to release.^[3,9] Thus, a theoretically ideal bifunctional catalyst that works for both ORR and OER processes should seek an overall balance of the adsorption free energies to the reactants and the intermediates of these two reactions.

2.2. Oxygen Electrocatalyst Evaluation

The performance of oxygen electrocatalysts is often examined by different electrochemical methods. In this section, we briefly introduce the fabrication of oxygen working electrodes, their main performance indicators (such as onset/over potential, potential gap, exchange current density, Tafel slope, electron transfer number, and turnover frequency) and device evaluation.

2.2.1. Working Electrode

The preparation of working electrode is a critical part in evaluating electrocatalytic performance of oxygen electrocatalysts. For both conventional powdery catalysts and newly developed freestanding electrode structures, the most fundamental electrochemical behaviors are usually obtained by loading the catalytic material onto the glassy carbon (GC) surface of a rotating disk electrode (RDE). Compared with a stationary working electrode, RDE can effectively maintain steady-state mass transport during oxygen reactions and provide fundamental information of reaction mechanism.

In a conventional electrode fabrication process, catalysts are mixed with carbon black powders, organic binder, and solvent to form a catalyst ink and then casted onto GC surface. The preparation of working electrode plays a critical role in determining the catalytic performance and dramatically influences the reaction rate due to the difference in structure, conductivity,

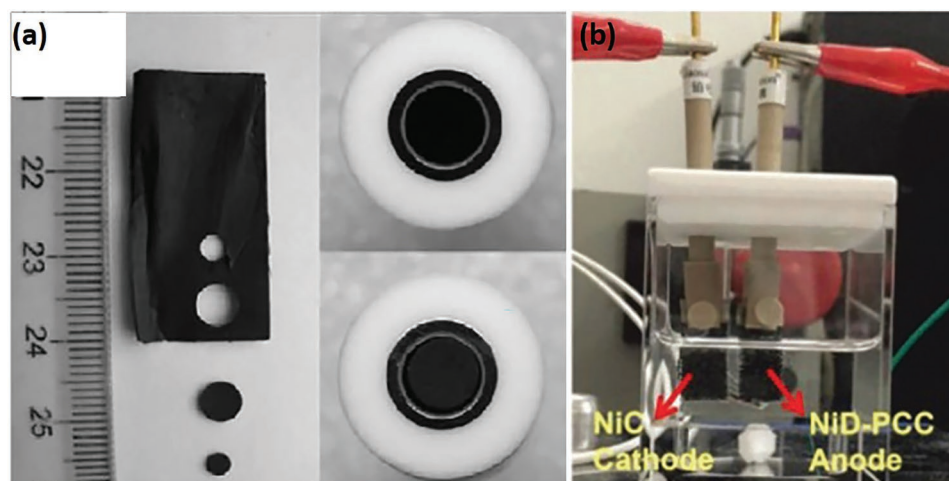


Figure 2. a) Disk-shaped carbon film for ORR test on RDE. Reproduced with permission.^[31] Copyright 2009, Royal Society of Chemistry. b) water splitting test for free-standing electrocatalyst. Reproduced with permission.^[32] Copyright 2016, Royal Society of Chemistry.

degree of wettability, and electrolyte accessibility of the catalyst.^[28] The use of organic binder normally results in poor wettability, catalyst powder agglomeration, and coverage of reactive sites on the electrode. Due to the highly compact structure of cast catalyst on working electrode, active catalytic layer tends to peel off from the electrode surface during OER test, when a large amount of oxygen is evolved, especially for these well-performing OER catalysts. To solve this problem, catalytic materials can be drop-casted onto a 3D conductive substrate like Nickel (Ni) foam or CC for OER measurement.

In addition to making catalyst ink for ORR/OER evaluation,^[29] freestanding catalytic structures can be cut to match the disk size of the RDE electrode and adhered to the electrode surface using Nafion solution, as shown in **Figure 2a**. This approach allows multiple pathways for electrolyte penetration and achieves effective utilization of entire electrode structure during catalytic reactions.^[30,31] However, the binder Nafion still increases the electrical resistance, blocks the active sites, and prevents ion diffusion. Moreover, it is even easier for the freestanding structure to be peeled off from the rotating electrode surface due to reduced contact area. Therefore, the freestanding structures are directly used as working electrode in some tests, without attaching onto a RDE surface.^[17,32–35] With reduced possibility of catalyst detachment from the electrode surface, it allows easier penetration of gas and electrolyte, resulting in higher catalytic efficiency and extended catalyst life time. Specifically, in Balogun's study of using CC as the matrix to synthesize OER catalyst, for the OER and overall water splitting electrode preparation (**Figure 2b**), the CC with a geometric area of 1.0 cm² and a small area at the other end for ohmic contact was clamped to a current collector. The active area was simply determined by the geometric area of CC. Thereby, all reported data were normalized by its geometric area.

2.2.2. Onset/Half-Wave/Over Potentials

The most significant factor in determining the catalytic performance of an oxygen electrocatalyst is onset potential. **Figure 3**

shows the polarization curve of the oxygen-involving reactions on an air cathode. So far, three different approaches have been applied for the determination of ORR onset potential:

- 1) Initially, the most common approach is to obtain the intersection value of the tangents between the rising current portion and the baseline of a voltammogram, as shown in **Figure 3**;
- 2) It is defined as the critical potential where the reduction current density reaches 1% of the limiting current density (j_L).
- 3) The ORR polarization curve is normally obtained by subtracting the data under N₂ from that under O₂ measured with identical experimental parameters, therefore, the onset potential can also be obtained at the value when the current in the O₂ curve starts to deviate from that in the N₂ curve.

Generally speaking, the first and the second methods give very close onset potential values. However, more researchers have used the second method in recent reports, because it is hard to define the tangent lines in some cases, and the second method has the advantage of simple arithmetic. However, it should be noted that the catalyst loading must be kept the same with the second method to obtain comparable limiting current density. Compared with the first two methods, the third method has been less frequently used due to its experimental complexity.

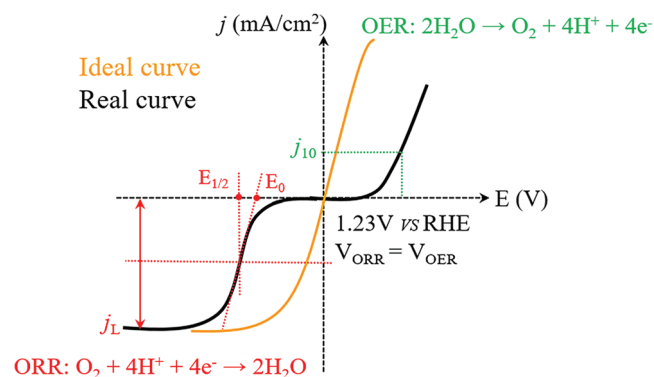


Figure 3. The polarization curve of oxygen-involving reactions at air cathode.

Because it is difficult to unify the exact onset potential, half-wave potential ($E_{1/2}$) is also regarded as an important criterion to evaluate ORR performance, which refers to the corresponding potential to the half of limiting current density j_L .

For OER evaluation, the potential value at 10 mA cm⁻² ($E_{j=10}$) is considered more reliable and more commonly used form comparison. Overpotential (η) is the potential difference between the potentials achieving a specific current density and the theoretical value of 1.23 V. For example, if a catalyst achieves $E_{j=10} = 1.63$ V, then it has an overpotential of 400 mV at 10 mA cm⁻². Generally, a catalyst with an overpotential in the range of 300–400 mV is considered to be good for OER.

2.2.3. Potential Gap (ΔE)

In addition to these general potential parameters, potential gap (ΔE) is a unique indicator to evaluate the performance of bifunctional ORR/OER catalyst. Normally, there are two methods for calculating this potential gap. It can be decided by the difference between the ORR potential at current density of -3 mA cm² and the OER potential $E_{j=10}$. Alternatively, the potential gap between the ORR half-wave potential ($E_{1/2}$) and the OER $E_{j=10}$ is sometimes used for evaluating the overall bifunctional activity. Attention should be paid that the ORR and OER polarization curves are required to be measured on similar catalyst loading for obtaining a trustworthy potential gap value.

2.2.4. Exchange Current Density (j_0)

For an electrochemical reaction, both forward and backward reactions can occur. At equilibrium, the current density of the forward reaction equals that of the backward reaction, which is called exchange current density (j_0). Exchange current density is one of the most important kinetic parameters to compare intrinsic catalytic activities. A large current density means that the system can deliver high currents even at very low overpotentials.

2.2.5. Tafel Slope (b)

When relating overpotential to the logarithm of current density (j), a linear portion can be found around the low-overpotential region, giving the Tafel equation

$$\eta = a + b \log(j) \quad (7)$$

Tafel slope (b) is another important parameter that indicates the reaction kinetics. A lower Tafel slope means a quicker increase in current density with the increment of overpotential, indicating faster reaction kinetics of the electrocatalyst.

2.2.6. Electron Transfer Number (n)

As aforementioned, 4e⁻ pathway is preferable in an ORR electrochemical reaction. Based on rotating ring-disk electrode

(RRDE) technique, the H₂O₂ yield and the electron transfer number can be calculated as follows

$$\text{H}_2\text{O}_2\% = 200 \times \frac{I_r/N}{I_d + I_r/N} \quad (8)$$

$$n = 4 \times \frac{I_d}{I_d + I_r/N} \quad (9)$$

where I_r is the ring current, I_d refers to the disk current, and N represents the collection efficiency.

In addition, the electron transfer number (n) can also be determined according to the Koutecký–Levich (K–L) equation derived from the ORR polarization curves with different rotation speeds

$$\frac{1}{j} = \frac{1}{j_k} + \frac{1}{j_d} = \frac{1}{j_k} + \frac{1}{0.62nFAD_0^{2/3}\nu^{-1/6}C_0}\omega^{-1/2} \quad (10)$$

where j is the experimentally measured current density, j_k and j_d are the kinetic and diffusion limited current densities, respectively. F is the Faraday constant (96 485 C mol⁻¹), ω refers to the electrode rotation rate which can be adjusted by the rotator, A represents the area of the glassy carbon electrode, D_0 is the diffusion coefficient of O₂ in the electrolyte (0.1 M KOH, 1.9×10^{-5} cm² s⁻¹), ν means the kinematic viscosity of the electrolyte (0.1 M KOH, 0.01 cm² s⁻¹), C_0 is the solubility of O₂ in the electrolyte (0.1 M KOH, 1.2×10^{-6} mol cm⁻³).

2.2.7. Electrochemically Active Surface Area (ECSA)

The ECSA is a precise measurement of the total number of active sites on a given surface for a certain reaction, which is especially essential for evaluating the intrinsic activity of Pt-based electrode. Experimentally, there are three main methods to determine the ECSA for both single component and hybrid materials:

- i) Under-potential deposition (UPD) hydrogen (H-UPD) adsorption method, which is widely applicable for Pt and Pt-based alloys

$$\text{ECSA} = \frac{Q_H}{m_{\text{Pt}} \times Q_f} \quad (11)$$

Where Q_H is the integrated charge of the hydrogen adsorption region from the CV curves, as shown in Figure 4a, Q_f is the required charge to adsorb a monolayer of hydrogen on a clean Pt surface, and its value is 0.21 mC cm⁻², m_{Pt} is the Pt mass loadings on the electrode.

- ii) CO stripping voltammetry, which is generally suitable for Ru and Ru-Pt alloy; and iii) Cu UPD stripping voltammetry, which can be used for a broader spectrum of surfaces like metal compounds. Similar calculation equations for ECSA are also applied for these two methods, with the integrated charge to be the CO stripping area for the second (Figure 4b) and the Cu stripping area for the third (Figure 4c), and the Q_f to be 0.42 mC cm⁻².^[36]

In terms of those nonplatinum catalysts, the ECSA can be evaluated based on the double-layer capacitance (C_{dl}), which

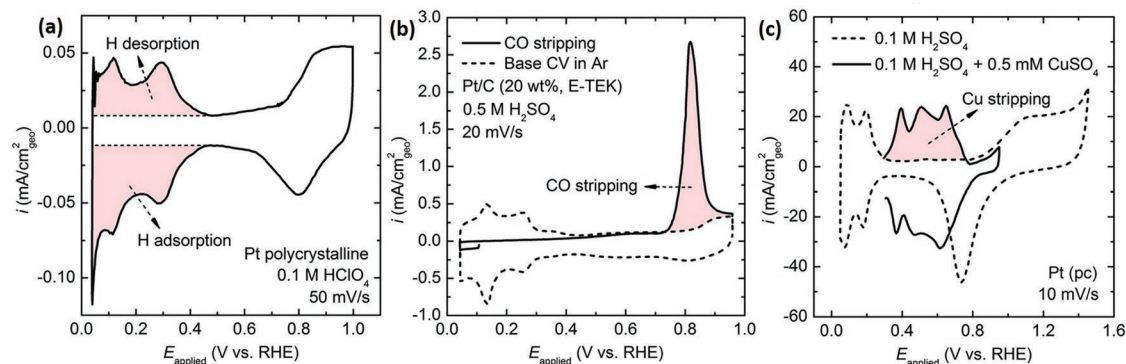


Figure 4. a) Hydrogen adsorption/desorption for measuring the surface area of polycrystalline Pt at 50 mV s⁻¹ in Ar-saturated 0.1 M HClO₄. b) CO stripping that quantifies the surface area of Pt/C at 20 mV s⁻¹ in Ar-saturated 0.5 M H₂SO₄. c) Under-potential deposition of Cu for measuring the surface area of Pt (pc). Reproduced with permission.^[36] Copyright 2018, Royal Society of Chemistry.

is measured by cyclic voltammetry (CV) tests. Specifically, CV test is performed at different scan rates in a potential window where no Faradaic process occurs. The plot of the $\Delta j = (j_a - j_c)$ against the scan rates has a linear relationship and the linear slope is twice of C_{dl} , where j_a and j_c refer to the anodic and cathodic currents.^[37,38]

2.2.8. Turnover Frequency (TOF)

TOF is always used to compare OER performance of different electrocatalysts. It is calculated from the following equation

$$\text{TOF} = (j \times A) / (4 \times F \times m) \quad (12)$$

where j is the current density at a given overpotential, A refers to the area of the working electrode, F represents the Faraday constant (96 485 C mol⁻¹), and m means the number of moles of the active materials.

2.2.9. Stability Evaluation

The stability of a catalyst is very important to practical application. There are basically two approaches for evaluating the stability of oxygen electrocatalysts. Most researchers carry out chronopotentiometry at a constant current density ($V-t$) or chronoamperometry at a constant potential ($I-t$) to inspect whether the prepared catalysts can sustain the potential or current for a long period of time. The other method is to compare the ORR/OER linear sweep voltammetry (LSV) curves before and after a large number of CV scans, usually over 1000, in the corresponding reduction or evolution regions.

2.2.10. Device Evaluation

Despite aforementioned fundamental parameters of oxygen electrocatalysts, it is worth noting that both liquid and all-solid-state devices are often constructed to practically demonstrate the electrocatalytic performance of freestanding electrodes, many with bifunctional ORR/OER activities.

Take Zn–air battery as an example, liquid Zn–air battery normally consists of a polished zinc plate as anode and a freestanding structure as air cathode, with 6 M KOH (primary Zn–air battery) or 6 M KOH + 0.2 M Zn(Ac)₂ (rechargeable Zn–air battery) sealed in between as the electrolyte.^[39–42] The only difference between all-solid-state and liquid Zn–air batteries is the electrolyte. Solid-state batteries use polymer gel electrolyte, which can be prepared using polyvinyl alcohol (PVA),^[43–45] polyacrylamine,^[46] polyacrylate (PAA),^[47] PVA/polyacrylic acid (PAA),^[48] etc. The electrolyte can be incorporated into a gel form during electrolyte solution preparation or through soaking the bare gel in electrolyte solution.

The performance evaluation of these devices can be primarily conducted using open-circuit voltage, charge and discharge polarization curves, Nyquist plots for the resistance, and galvanostatic discharge–charge cycling test for device stability.

3. Oxygen Electrocatalysts Derived from Fibrous Organic Sources

Different from anchoring electrocatalyst powders onto pre-existing conductive substrates, fibrous organic materials can be mixed with active ingredients and converted to freestanding oxygen electrocatalysts through controlled carbonization process, during which catalytic sites are generated simultaneously with the formation of graphitic fibrous carbon or other inorganic fibrous structures. This fabrication approach has attracted growing research attention due to its wide range of fiber selection, low material cost, controllable electrode structure, and easy fabrication. So far, four different types of organic fibrous structures have been exploited to prepare freestanding fibrous oxygen electrodes: electrospun nanofiber webs, bacterial cellulose aerogels, cellulose fibrous structures, and other organic species.

3.1. Electrospun Nanofibers

Electrospinning is a fiber making method that uses electrostatic force to draw electrically charged thread of polymer solutions or polymer melts to ultrafine fibers with an average diameter

of several hundred nanometers. Electrospinning can efficiently prepare nanofibers from a wide range of polymeric materials, with controllable fiber morphology and fibrous structure. Electrospun nanofiber webs have been the most widely used fibrous structure for oxygen electrode. So far, the polymers that have been electrospun for this application include polyacrylonitrile (PAN), polyvinylpyrrolidone (PVP), PAA, polyimide (PI), and some polymer composites.

3.1.1. PAN

PAN is the most widely used precursor material in commercial carbon fiber production. With the in-depth knowledge generated from carbon fiber industry, PAN nanofiber-derived carbon nanofibers have been intensively explored as electrode material in different energy devices.

PAN was initially examined as a carbon support for Pt-Pd alloy nanoparticles. When the nanoparticle loading was 1.85 mg cm^{-2} , a maximum peak ORR potential of 0.24 V in cyclic voltammogram was obtained in 0.1 M HClO_4 .^[49] For replacing noble metal electrocatalysts with low-cost materials, more recent research efforts have been devoted to searching efficient non-noble metals and heteroatom-doped carbon materials. Based on the critical role of heteroatom doping in oxygen catalysis, Yu's group prepared nitrogen-doped carbon nanofibers for oxygen reduction catalysis by first stabilizing electrospun PAN nanofibers in air at 250°C , followed by the carbonization of stabilized nanofibers in NH_3 or a two-step carbonization process consecutively in N_2 and NH_3 .^[50,51] It was believed that the enhanced ORR performance was attributed to the increased porosity and pyridinic-N content. Following this work, the effect of different nitrogen sources, including melamine, aniline, urea and polyaniline, on ORR performance was further investigated, and the aniline/PAN mixture exhibited the best activity.^[52] Jindal and Chen, respectively, tried to obtain metal-free ORR catalysts by adding carbon nitride into the electrospinning solution or conducting KOH activation to carbonized PAN nanofibers.^[53,54]

Inspired by the early demonstration of electrocatalytic activity of metal chelate (CoPc) in 1960s,^[55] many subsequent studies have concluded that pyrolyzed transition metal and nitrogen compounds supported on carbon species (M/N/C) can provide efficient active sites and achieve significantly improved ORR property. Therefore, different metal salts and N-containing substances have been integrated into PAN nanofibers. **Figure 5a** depicts the preparation of Fe_3C @nitrogen doped CNT arrays aligned on nitrogen-doped carbon nanofibers (Fe_3C @NCNTs-NCNFs). $\text{Fe}(\text{acac})_3$ was first mixed into the PAN solution to fabricate composite electrospun nanofibers, followed by a stabilization process and a carbonization treatment in the presence of melamine to achieve fibrous Fe_3C @NCNT aligned arrays on the carbon nanofiber substrate, as shown in **Figure 5b**.^[56] This nanofibrous material exhibited an outstanding OER activity with a low overpotential of 284 mV at 10 mA cm^{-2} , even surpassing the commercial RuO_2 catalyst (**Figure 5c**). Moreover, the polarization curve remained almost the same as that of the initial test after 5000 cycles, indicating excellent durability. The free-standing materials directly utilized as working electrode

are normally more stable compared to the pasted electrodes, because it not only eliminates the peeling off problem of catalyst layer, but also avoid the use of any additional binders which affects electron transfer efficiency during the reaction.

More details of the carbonized freestanding electrospun nanofiber webs with M/N/C compounds have been summarized in **Table 3**, including different precursors, synthesis methods, and relevant ORR/OER performance.

In order to further improve the electrical conductivity and surface area of carbon nanofibers, graphene nanoplatelets, and graphene oxide were, respectively, incorporated into PAN solutions for electrospinning, together with iron salts.^[70,71] After similar stabilization and carbonization processes, the ORR performance of these composite carbon nanofibers were almost comparable or even superior to commercial Pt/C catalyst. Through XPS analysis, the ratio between Fe and N (pyridinic + pyrrolic) was determined as $0.44:1.78$ ($\approx 1:4$), offering strong evidence of the formation of Fe-N_4 structure, which has been considered as the active ORR site.

In addition to nitrogen, other heteroatoms (such as B and P) can also have doping effect for oxygen catalysis. A 3D porous B, N-codoped carbon nanofiber web was prepared by pyrolyzing precarbonized electrospun PAN nanofibers with boric acid and urea in N_2 , followed by an activation treatment in NH_3 . The NH_3 treatment gave the nanofibrous carbon structure a specific surface area of $306.3 \text{ m}^2 \text{ g}^{-1}$, which was 30 times higher than that of undoped carbon fiber. The carbon nanofibers had a hierarchical structure with both micro- and mesopores, providing sufficient sites to form B, N/C compounds, with an ORR onset potential only 60 mV more negative than Pt/C.^[72] In addition, core-sheath nanofibers were prepared by photopolymerizing polythiophene on electrospun $\text{PAN/C}_3\text{N}_6\text{H}_6/\text{FeCl}_3$ nanofibers, and subsequent stabilization and carbonization processes led to the formation of Fe-S/N-C catalyst, which exhibited an ORR onset potential of 0.94 V .^[73] Using an in situ growth approach, Fe/Ni alloy nanosheets were first electrodeposited onto the surface of electrospun carbon nanofibers, then the composite structure was phosphatized at 300°C with NaH_2PO_2 (**Figure 5d**).^[57] The SEM image in **Figure 5e** reveals that Fe/Ni/P ultrathin sheet arrays were uniformly and vertically grown on the nanofibers. The freestanding 3D electrode showed an OER overpotential as low as 215 mV at 10 mA cm^{-2} in 1 M KOH (**Figure 5f**). In addition, the chronopotentiometry test showed that there was only a potential decrease of 35 mV at a current density of 10 mA cm^{-2} after 10 000 CV cycles.

Recently, bifunctional oxygen catalysts toward both ORR and OER have attracted more attention for rechargeable energy storage devices, and many transition metal oxides have been carefully investigated. Cobalt oxides were introduced onto carbon nanofibers by an air annealing treatment of electrospun $\text{Co}(\text{OAc})_2/\text{PAN}$ nanofibers.^[74,75] The testing results of rechargeable metal-air batteries suggested that they could have long-term durability by charging for 12 h at 60 mA cm^{-2} and discharging for 8 h at 80 mA cm^{-2} . A thin-walled bimetal oxides catalyst ($\text{CuCo}_2\text{O}_4/\text{C}$) was fabricated via a coaxial electrospinning technique, as shown in **Figure 5g**.^[58] The SEM images (**Figure 5h,i**) show that the $\text{CuCo}_2\text{O}_4/\text{C}$ nanotubes were continuous and had abundant pores on the rough tube surface,

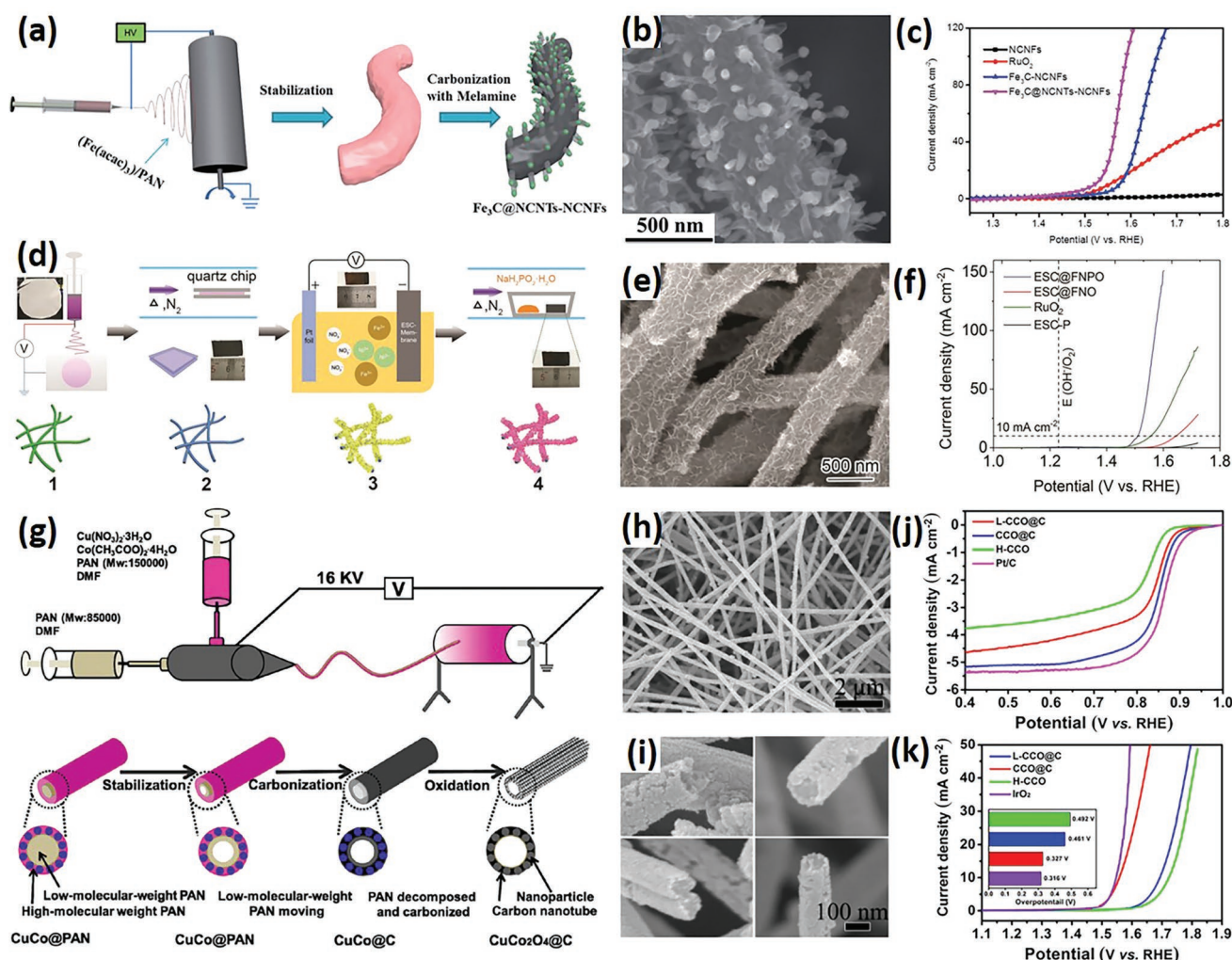


Figure 5. a) Schematic illustration of the fabrication of Fe₃C@NCNTs-NCNFs. Reproduce with permission.^[56] Copyright 2017, Royal Society of Chemistry. b) SEM image of Fe₃C@NCNTs-NCNFs. c) OER polarization curves of Fe₃C@NCNTs-NCNFs and RuO₂ in 1 M KOH. d) Schematic illustration of the fabrication of electrospun carbon nanofibers integrated with ultrathin iron–nickel phosphate nanosheet (ESC@FNPO). Reproduced with permission.^[57] Copyright 2017, John Wiley and Sons. e) SEM image of ESC@FNPO. f) OER polarization curves of ESC@FNPO in 1 M KOH. g) Schematic illustration of the preparation of CuCo₂O₄@C Nanotubes. Reproduced with permission.^[58] Copyright 2017, American Chemical Society. h,i) SEM images of CuCo₂O₄@C nanotubes. j,k) ORR polarization curves CuCo₂O₄@C nanotubes in 0.1 M KOH and their OER polarization curves in 1 M KOH.

which could improve the diffusion kinetics of hydroxide and favor the transportation of oxygen during ORR process. This material exhibited an ORR onset potential of 0.95 V and an overpotential of 327 mV at 10 mA cm⁻² in 0.1 M KOH (Figure 5j,k). Significantly, when assembled in Zn–air batteries, this kind of catalyst displayed a low charge–discharge voltage gap (0.79 V at 10 mA cm⁻²) and a long cycling life (up to 160 cycles for 80 h).

Metal sulfides and phosphides can also be developed as bifunctional catalysts. Wang et al. reported a manganese sulfide and cobalt (MnS/Co) encapsulated nanofibrous web as free-standing air electrode, using cobalt and manganese acetate as the metal sources, and thiourea as the sulfur source in the PAN solution.^[76] Experimental results have confirmed that both ORR and OER performance of the nanofibrous material were comparable to those of commercial catalysts. Surendran et al. applied nickel and cobalt nitrates, together with red phosphorous to

the electrospinning solution.^[77] Through a typical stabilization and carbonization process, the obtained NiCoP/CNF structure exhibited outstanding oxygen electrocatalytic results with an ORR onset potential of 0.82 V and an OER overpotential of 268 mV at 10 mA cm⁻² in 0.1 M KOH.

As a special crystalline form of microporous material containing both metal atoms and functional groups, metal–organic frameworks (MOF) have been increasingly applied in different catalytic fields. Liu et al. first synthesized Zn, Co-zeolitic imidazolate framework (Zn, Co-ZIF) using a solvothermal reaction of Zn(NO₃)₂, Co(NO₃)₂, and 2- methylimidazole (MIM) in methanol.^[78] Then the Zn, Co-ZIF particles, and Co(NO₃)₂ were dispersed in a PAN/DMF solution to prepare electrospun composite nanofiber webs, followed by carbonization and acid leaching treatment. This novel catalyst exhibited very close ORR performance to commercial Pt/C with a half-wave potential of 0.83 V, ascribed to a synergistic effect between large specific

Table 3. A summary of recently reported M/N/C oxygen electrocatalysts fabricated through electrospinning.

Materials	Methods	Electrolyte	Onset potential [V vs RHE]	Electron transfer number [<i>n</i>]	<i>I</i> - <i>t</i> response	Ref.
Fe-N/CNF	Three-step annealing of FeC ₂ O ₄ /PAN/ nanofibers: 1. Preoxidized in air; 2. Carbonized in N ₂ ; 3. Carbonized in NH ₃ .	0.5 M H ₂ SO ₄	ORR: 0.90	3.91 @0.50 V	80% after 18 h	[59]
Co-N-CNF	Two-step annealing of Co(NO ₃) ₂ /PAN nanofibers: 1. Stabilized in air; 2. Carbonized in N ₂ .	0.1 M KOH	ORR: 0.87	3.70 @0.37 V	—	[60]
Fe-N/CNF	Air stabilized PAN nanofiber impregnated in Fe(NO ₃) ₃ , followed by carbonization in NH ₃ .	0.1 M KOH	ORR: 0.97	3.93 @0.57 V	94% after 5.6 h	[61]
		0.5 M H ₂ SO ₄	ORR: 0.81	3.98 @0.40 V	83% after 5.6 h	
NCNT/CNFs	Three-step annealing of Fe(Ac) ₂ /PAN nanofibers: 1. Stabilized in air; 2. Carbonized in H ₂ /N ₂ ; 3. Carbonized with pyridine in N ₂ .	0.1 M KOH	ORR: 0.91	3.80 @0.57 V	95% after 2.8 h	[62]
Fe-PANI-PAN	Two-step annealing of Fe-PANI+FeCl ₃ / PAN nanofibers: 1. Stabilized in air; 2. Carbonized in Ar.	0.1 M HClO ₄	ORR: 0.90	3.89 @0.65 V	—	[63]
TM-CNFs	Two-step annealing of Fe/Co/Ni acetylacetonate/ PAN nanofibers: 1. Stabilized in air; 2. Carbonized in N ₂ .	0.1 M KOH	ORR: Ni-CNF 0.80 Fe-CNF 0.92 Co-CNF 0.90	—	—	[64]
Fe-N-C	Two-step annealing of Fe(NO ₃) ₃ /PAN nanofibers: 1. Stabilized in air; 2. Carbonized in Ar/O ₂ .	0.1 M HClO ₄	ORR: 0.88/0.82	3.99 @0.65 V	70% after 4.7 h 92% after 6.9 h	[65,66]
Co-PAN-800	Two-step annealing of Co(C ₅ H ₇ O ₂) ₃ /PAN nanofibers: 1. Stabilized in air; 2. Carbonized in Ar.	0.1 M KOH	ORR: 0.85	3.87 @0.57 V	—	[67]
Fe ₃ C@NCNTs-NCNFs	Two-step annealing of Fe(acac) ₃ /PAN nanofibers: 1. Stabilized in air; 2. Carbonized with melamine in Ar.	1 M KOH	OER: 1.39	—	—	[56]
Fe-N/C	Two-step annealing of Fe(acac) ₃ /PVP nanofibers: 1. Stabilized in air; 2. Carbonized with g-C ₃ N ₄ in N ₂ . H ₂ SO ₄ +Water wash, followed by the third carbonization.	0.5 M H ₂ SO ₄	ORR: 0.86	4.04 @0.55 V	91% after 4.2 h	[68]
HP-Co-NCNFs	Two-step annealing of Co(Ac) ₂ /PVP nanofibers: 1. Stabilized in air; 2. Carbonized in N ₂ .	0.1 M KOH	ORR: 0.91	3.9 @0.42 V	91% after 11.1 h	[69]

surface area (515.2 m² g⁻¹) and high degree of graphitization. Meanwhile, another Zn, Co-ZIF/PAN core-sheath catalyst was prepared by dipping MIM/PAN nanofibers into Zn(NO₃)₂ and Co(NO₃)₂ solutions for Zn, Co-ZIF growth on the fiber surface.^[79] Finally, the carbonized Zn, Co-ZIF/PAN nanofibers delivered a half-wave ORR potential of 0.77 V.

Different from the deposition of pre-prepared MOF particles onto nanofibers, in situ growth of MOF materials on nanofiber surface has also been achieved. After preparing a carbon nanofiber template decorated with Co-ZIF particles, Ji et al. first combined MoS₂ onto this template by a hydrothermal treatment with (NH₄)₂MoS₄ to obtain CoNC@MoS₂/CNF catalyst for water splitting.^[81] Afterward, acid leaching was also performed on the template, leading to the formation of a bifunctional catalyst with single cobalt atoms (Co SA@NCF/CNF), as shown in Figure 6a,b.^[80] The SEM image of Co SA@NCF/CNF catalyst in Figure 6c shows that the carbon flakes derived from Co-ZIF uniformly covered the carbon nanofiber surface and the open mesopores on the flakes (inset of Figure 6c) were well retained. After acid etching, the Co clusters were completely removed (Figure 6d), leading to the formation of abundant

mesoporous structures. Due to the optimized single-atom active sites and facile construction of hierarchically porous architectures, the binder-free Co SA@NCF/CNF exhibited excellent electrocatalytic activities with a reversible oxygen overpotential of 0.75 V in alkaline medium (Figure 6e,f). Notably, this material in zinc-air battery possessed excellent stability as there was no obvious change in charge and discharge voltages over 90 cycles, which was much better than the Pt/C+Ir/C//CC-based battery.

3.1.2. PVP

Different from PAN, PVP is easy to decompose at high temperature. Therefore, PVP is often electrospun into nanofibrous structures to function as a sacrificing template during carbonization process, leaving the active materials with nanofibrous morphology. Initially, noble metals like Pt, PtPd nanotubes, and Pt-Fe alloy nanowires were successfully fabricated through mixing metal salts into PVP solutions, followed by a controlled carbonization.^[82–84] The results showed that

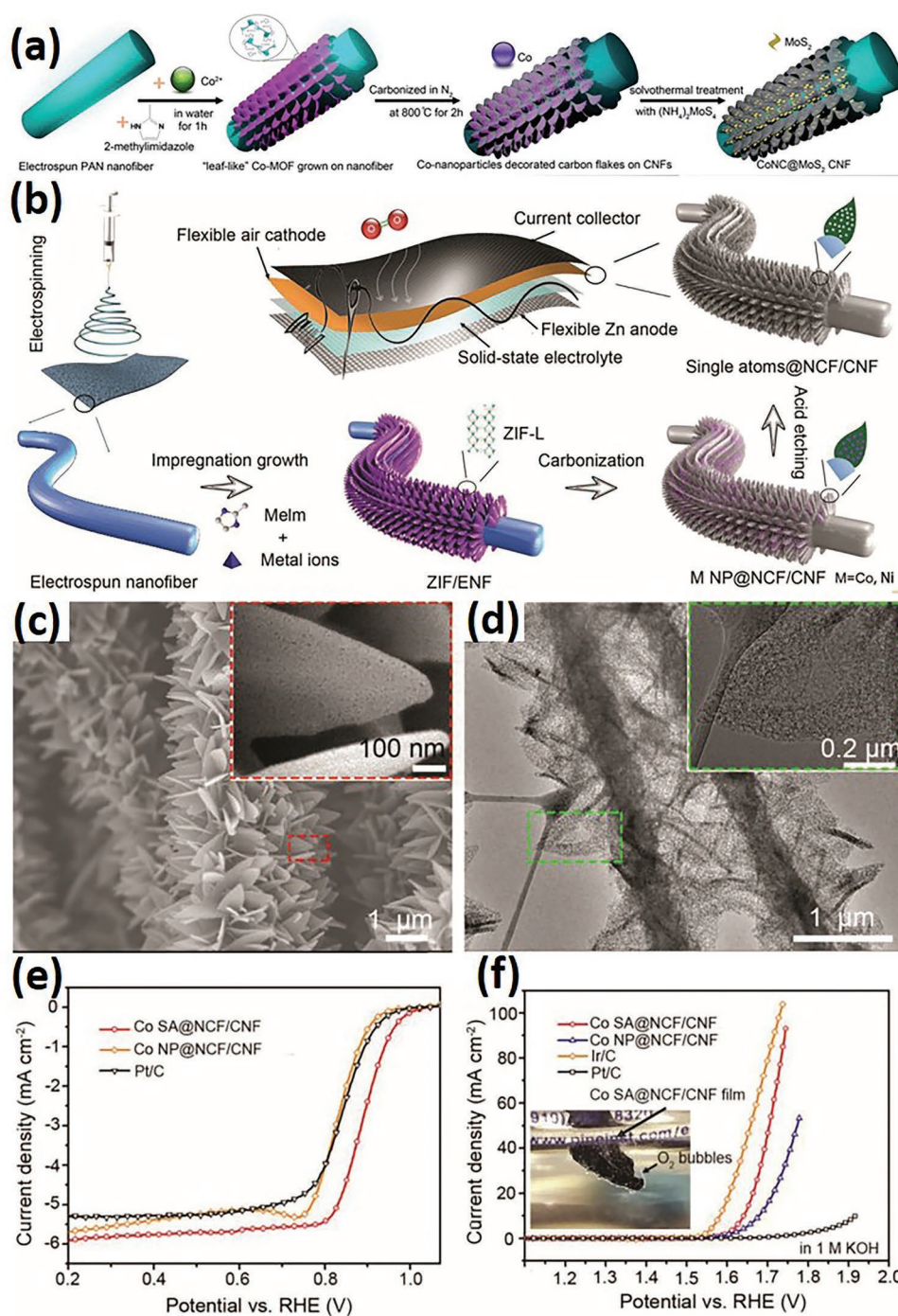


Figure 6. Schematic illustration of the fabrication of freestanding a) CoNC@MoS₂/CNF and b) Co SA@NCF/CNF webs. Reproduced with permission.^[80,81] Copyright 2017, Royal Society of Chemistry; and Copyright 2019, John Wiley and Sons. c) SEM and d) TEM images of Co SA@NCF/CNF. e) ORR polarization curves in 0.1 M KOH and f) OER polarization curves in 1 M KOH of Co SA@NCF/CNF.

they exhibited comparable or superior ORR catalytic properties to Pt/C catalyst. For developing low-cost non-noble metal catalysts, tungsten carbide (WC) nanofibers with diameters of ≈50 nm were successfully synthesized for ORR application.^[85] A three-step carbonization process was used to conduct thermal treatments on ammonium-meta-tungstate/PVP composite nanofibers in the turns of O₂, CH₄/H₂, and NH₃. Moreover,

AgCo composite nanotubes were synthesized by depositing a Ag layer on Co nanotubes with a galvanic replacement reaction method, in which the Co nanotubes was obtained by a two-step calcination of Co/PVP nanofibers in air and H₂/Ar.^[86] The composite AgCo nanotubes achieved better ORR activity than bare Pt and comparable performance to Pt/C, while exhibiting a higher level ethanol tolerance.

With nanofibrous PVP template, many studies have been carried out on the preparation of 1D metal oxide structures.^[87,88] Using a simple postannealing treatment, Li et al. prepared electrospun $\text{La}_{0.5}\text{Sr}_{0.5}\text{CoO}_{2.91}$ nanotubes as bifunctional cathode for rechargeable $\text{Li}-\text{O}_2$ batteries.^[89] With a similar fabrication strategy, hollow $\text{RuO}_2/\text{Mn}_2\text{O}_3$ composite fibers exhibited comparable ORR electrocatalytic performance to Pt/C catalyst with a close half-wave potential.^[90]

More recently, solution blow-spinning (SBS) technique has been exploited as a novel micro and nanofiber production strategy. Instead of the requirement of high electric field during electrospinning, SBS uses pressurized airflow to shrink polymer solution jet, which largely decreases the energy consumption. Different metal oxide hollow nanofibers were successfully synthesized by Macedo's group with this method using PVP as the sacrificing template, and exhibited promising OER performance.^[91–93]

Different from complete decomposition of PVP at high temperature thermal treatment, PVP can be partially remained during a lower temperature synthesis to become carbon substrate.^[94] Li et al. applied a two-step annealing process (air stabilization at 250 °C, then N_2 heating at 600 °C) to the Co and Fe containing PVP nanofibers, and the resulted composite material exhibited excellent OER performance with a potential at 10 mA cm^{-2} only 7 mV negative than commercial RuO_2 catalyst.^[95]

3.1.3. Other Polymers

In addition to PAN and PVP, other polymers have also been electrospun into nanofibers for the preparation of oxygen electrocatalytic structures. For example, Miao et al. prepared a composite carbon nanofiber web from PAA nanofibers coupled with nanocubic- Co_3O_4 for efficient ORR catalysis.^[96] The onset potential and current density were greatly improved when compared with pure carbon nanofibers without cobalt oxides, but still inferior to commercial Pt/C catalyst.

Moreover, polyvinylidene fluoride (PVDF)/ FeCl_3 @PPy core-shell fibers were fabricated by chemical vapor phase polymerization of pyrrole on electrospun PVDF/ FeCl_3 fibrous substrate.^[97] The polypyrrole (PPy) shell acted not only as nitrogen source, but also a protective layer for the active Fe_3C substance, giving long-term stability and efficient ORR performance in both alkali and acid media.

By adding a functional material, Liu et al. prepared PI nanofibers using a typical electrospinning process and turned them to carbon nanofibers in Argon (Figure 7a).^[45] The carbon nanofiber web prepared at 1000 °C (NCNF-1000, Figure 7b) showed a typical 3D randomly entangled fibrous network structure with a thickness of $\approx 60 \mu\text{m}$. Impressively, this carbon nanofiber web had a specific surface area of $1249 \text{ m}^2 \text{ g}^{-1}$, with the onset potential of both ORR and OER processes reached the same level of commercial catalysts, as shown in Figure 7c,d. Both primary and all-solid-state rechargeable Zn–air batteries were assembled to demonstrate the practical application of this carbon nanofiber web. Figure 7e shows the discharge and charge polarization curves of the primary Zn–air batteries. Compared to Pt/C, a slightly lower charge–discharge voltage

gap was observed for NCNF-1000, indicating a better rechargeability. The flexible all-solid-state Zn–air batteries composed of freestanding NCNF-1000 air cathode, zinc foil anode and alkaline PVA gel electrolyte, as shown in Figure 7f. Figure 7g exhibits that series-connected solid Zn–air batteries could be used to power a blue LED (3.0 V) without obvious performance decay even when the cells were bent to a large angle or folded (Figure 7h). Moreover, in the galvanostatic discharge–charge cycling test for the NCNF-1000 liquid ZAB, it showed a small increase in the voltage gap by 0.13 V after 500 cycles, whereas Pt/C demonstrated a significantly higher increase in the voltage gap (0.38 V) under the same condition.

Recently, with the help of atomic layer deposition method, Patil et al. prepared $\text{NiOOH}/\text{Ni}(\text{OH})_2$ decorated polymer of intrinsic microporosity carbon fibers.^[98] The synergistic effect among high surface area carbon, nitrogen doping, and Ni compounds endowed the freestanding cathode with an OER overpotential of 391 mV at 10 mA cm^{-2} and long-term stability.

3.1.4. Polymer Composites

Although electrospun structures have demonstrated encouraging catalytic performance as oxygen electrode, carbon nanofibers made from a single type of polymer sometimes have limited surface area and lack of surface features. By using more than one polymer during electrospinning, composite nanofibers can be used to prepare highly porous carbon nanofibers.^[99,100]

The most intensively investigated system is PAN/PVP composite. Different metal salts have been added into the mixture solution to prepare metal alloy or metal oxide catalysts. By this strategy, Zhen et al. reported a $\text{La}_{0.6}\text{Sr}_{0.4}\text{Co}_{1-x}\text{Fe}_x\text{O}_{3-\delta}$ OER catalyst by a simple air carbonization of as-spun metal nitrates containing PAN/PVP nanofibers.^[101] Peng et al. further doped sulfur into carbonized CaMnO_3 @PAN/PVP nanofibers by calcinating as-spun precursor nanofibers with sulfur powders.^[44] It was revealed that the sulfur doping not only increased the electrical conductivity, but also provided more active sites. The obtained carbon nanofibers exhibited better ORR and OER activities than nondoped nanofibrous material. In another work, NiCo alloy nanoparticles decorated on electrospun PAN/PVP template also demonstrated outstanding bifunctional properties with a typical electrospinning and carbonization treatment in N_2 .^[102] Both ORR and OER performance were comparable or even superior to those commercial ones, which was mainly attributed to the synergetic effect between NiCo nanoparticles and nanofibrous carbon matrix.

In addition, some other sacrificial polymers have also been used in electrospun materials. Park et al. blended polystyrene (PS) into a PAN solution for electrospinning. During the following carbonization process, the PS particles helped to form a special porous structure with a high specific surface area of $1271 \text{ m}^2 \text{ g}^{-1}$. Excellent ORR performance with a four-electron pathway was found on the porous carbon nanofibers.^[103] Yu's group first prepared PAN-PVDF/silicon oil composite fiber by coaxial electrospinning technique.^[104] Then the subsequent NH_3 heat treatment contributed to the decomposition of PVDF. In comparison with the sample treated in N_2 ,

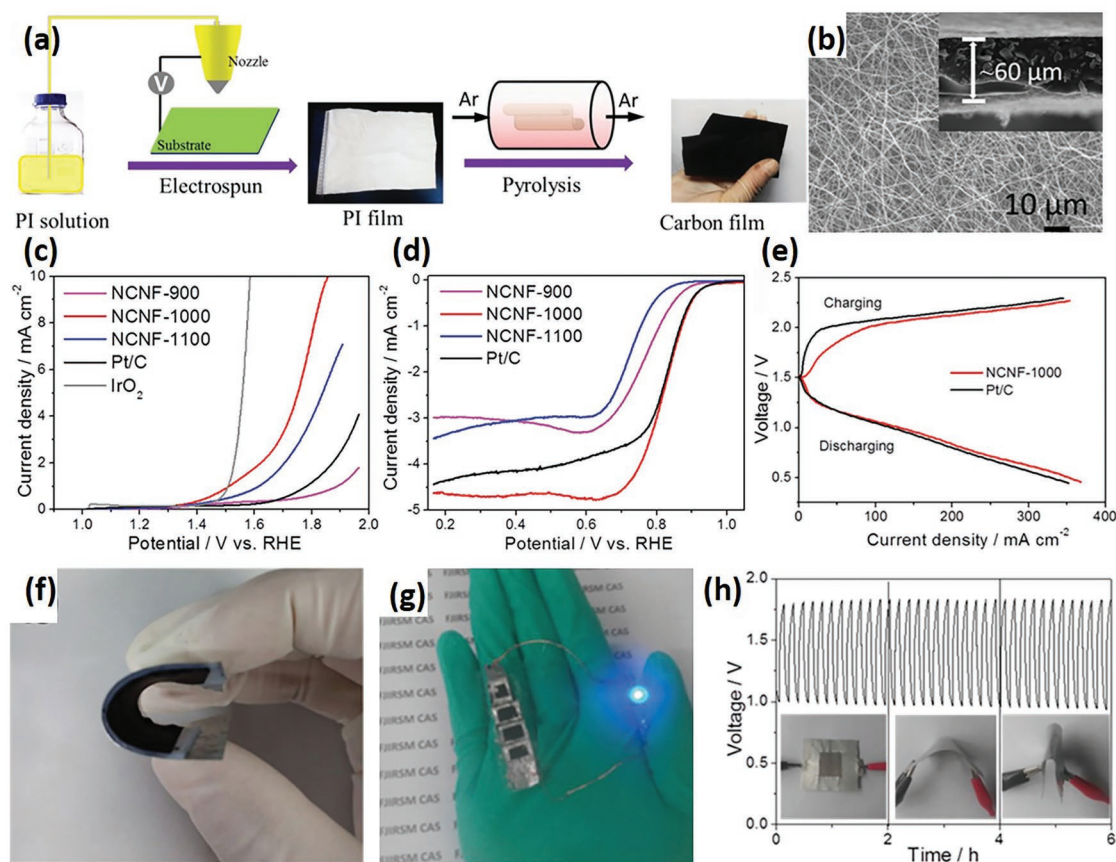


Figure 7. a) Schematic illustration of the fabrication of freestanding nanoporous carbon nanofiber webs (NCNF) using electrospun PI nanofibers. Reproduced with permission.^[45] Copyright 2016, John Wiley and Sons. b) SEM image of NCNF. c) ORR and d) OER polarization curves of NCNF in 0.1 M KOH. e) Charge and discharge polarization curves of primary Zn–air batteries with NCNF as air cathode. f) Photograph of the all-solid-state rechargeable Zn–air battery with NCNF as air cathode. g) Photographs of a blue LED (3.0 V) powered by four all-solid-state Zn–air microbatteries in series. h) Galvanostatic discharge–charge cycling curve at 2 mA cm^{−2} of the all-solid-state rechargeable Zn–air battery with NCNF as air cathode, with a bending strain applied for every 2 h.

the NH₃-etched nanofibers had a smaller diameter of about 350 nm and showed much better electrocatalytic ORR activity in acid media.

Later on, cellulose acetate (CA), PVP, and poly (methyl methacrylate) (PMMA) were also, respectively, mixed with PAN to prepare carbon nanofibers, followed by acid oxidation and NH₃ etching.^[105] Recently, Cao and co-workers used AgNO₃/PMMA as the core solution and Co(CH₃COO)₂/PAN as the shell solution for coaxial electrospinning.^[106] After peroxidation and carbonization, the PMMA components were decomposed to form hollow channels within carbon nanofibers, which also contained Co/CoO and Ag nanoparticles (AgNPs). This hierarchically porous freestanding nanofiber structure exhibited good capability and stability for Li–O₂ batteries.

Ji et al. dissolved Fe(acac)₃ into a PAN/CA solution, and by adjusting the weight ratio between PAN and CA, a porous and channel-rich structure was obtained since CA was decomposed during the carbonization process.^[107] This binder-free Fe₃C embedded Fe/N nanofiber catalyst could enable fast mass transport during electrochemical reaction and possessed an ORR half-wave potential of 12 mV more positive than that of Pt/C.

3.2. Bacterial Cellulose

Bacterial cellulose (BC) is a typical biomass material that can be produced on industrial scales via microbial fermentation. It is a low-cost and environmentally friendly material with abundant natural resource. Taking advantages of interconnected 3D networks of native cellulose-I nanofibers and excellent mechanical properties, BC structures have been utilized to prepare ultra-light and flexible carbon nanofiber aerogels, which possess high electrical conductivity and catalytic activity for oxygen catalysis.

In early studies, noble metals like Ag and Pt were immobilized onto BC through physical mixing and subsequent freeze-drying or hydrothermal techniques.^[108–110] Later, N-doped carbon nanofiber aerogels were obtained through a two-step pyrolysis successively in N₂ and NH₃ of the lyophilized BC, as shown in Figure 8a.^[111,112] Except for getting nitrogen source from NH₃ gas, Ye et al. reported a novel “vein-leaf” carbon structure through simple calcination of a mixture of urea and BC, in which urea acted as both the nitrogen source and the precursor for the layered graphitic carbon nitride (g-C₃N₄).^[113] Such 3D network was favorable for electron transfer and mass diffusion during an ORR process. Another N-doped CNF

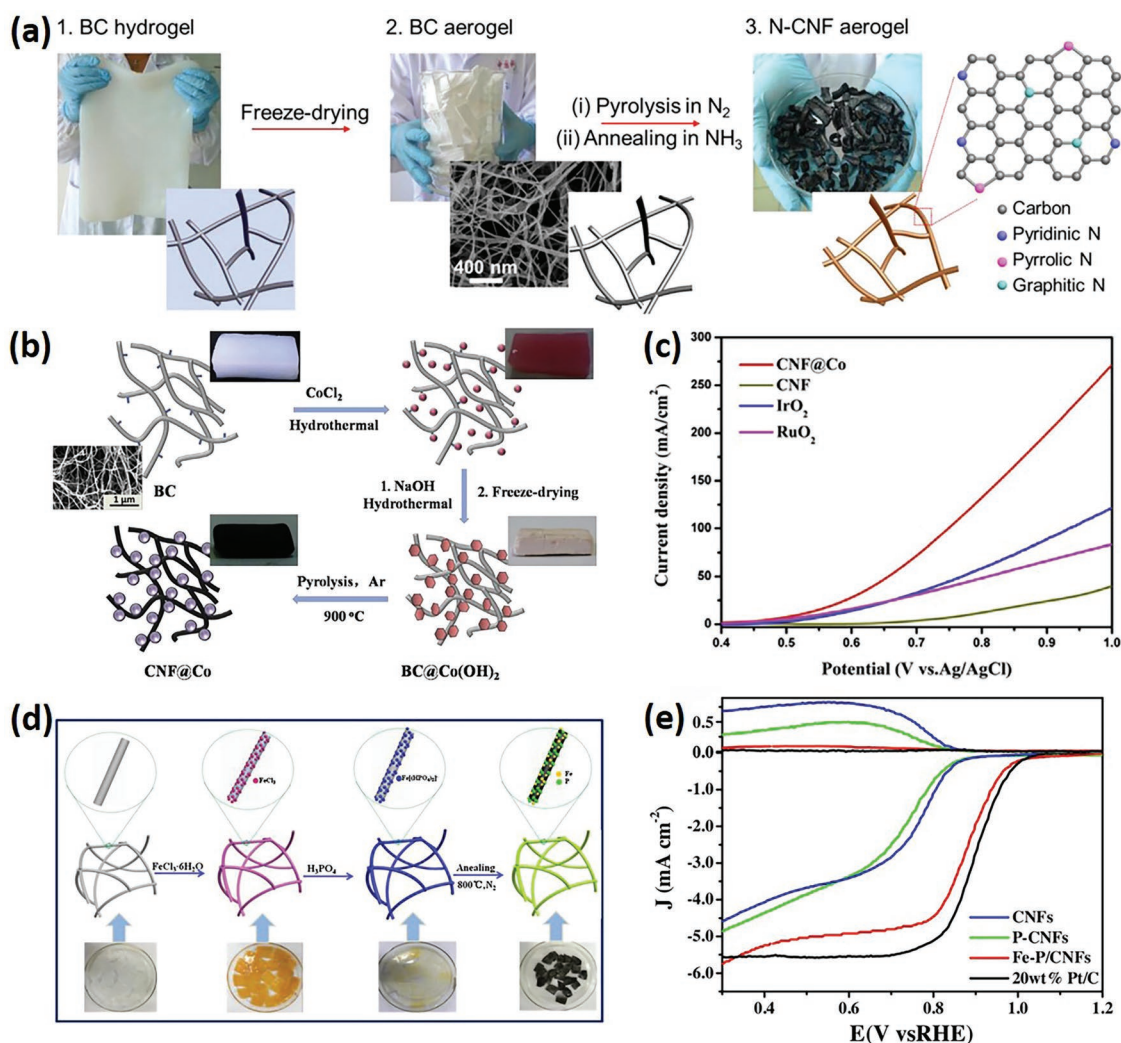


Figure 8. a) Schematic illustration of the fabrication of nitrogen-doped carbon nanofiber (N-CNF) aerogel. Reproduced with permission.^[112] Copyright 2015, Elsevier. b) Schematic illustration of the fabrication of CNF coated with Co nanospheres (CNF@Co). Reproduced with permission.^[116] Copyright 2015, Elsevier. c) OER LSV plots of CNF, CNF@Co, RuO_2 , and IrO_2 in 1.0 M KOH. d) Schematic illustration of the fabrication of Fe-P/CNFs. Reproduced with permission.^[117] Copyright 2017, Elsevier. e) ORR LSV and RRDE curves of Fe-P/CNF in 0.1 M KOH.

catalyst was synthesized by carbonizing PPy coated BC, and it was demonstrated that the pyridinic-N (2.95%) played a vital role in enhancing ORR performance.^[114] Recently, nitrogen and sulfur codoped carbon nanofibers (N/S-CNF) were prepared via an in situ chemical oxidative polymerization of methylene blue on bacterial cellulose nanofibers, followed by a carbonization process.^[115] The nanofibrous material displayed high ORR activity in alkaline media with a half-wave potential of about 0.80 V.

Transition metals can be used to further enhance the oxygen catalytic performance of BC-derived carbon nanofibrous structures. Initially, Cao et al. prepared cobalt-based nanosphere decorated CNF network, which had an OER overpotential of 310 mV at a current density of 10 mA cm⁻².^[116] The $Co(OH)_2$ nanoplates were first introduced to the BC hydrogel by hydrothermal treatment, followed by freeze-drying and annealing processes, as shown in Figure 8b. The as-prepared CNF@Co catalyst showed excellent OER activity with a low overpotential

of 314 mV at a current density of 10 mA cm⁻² (Figure 8c). My mixing $CoCl_2$, thiourea and urea to a BC template, CoO nanoparticles embedded N/S co-doped CNF was obtained, which exhibited an ORR onset potential of 0.84 V and an OER overpotential of 0.22 V at a current density of 10 mA cm⁻².^[118]

Liu et al. developed BC-based carbon nanofibers with $CoFe_2O_4$ nanoparticles (CFO/CNF), which worked as an active catalyst for both ORR and OER.^[119] First, Fe^{3+} and Co^{2+} were absorbed onto lyophilized BC aerogels and then reduced by ammonium hydroxide in a hydrothermal treatment. The following pyrolysis process at 500 °C led to the crystallization of $CoFe_2O_4$ nanoparticles and the carbonization of BC. Iron and phosphorous co-doped carbon nanofibers (Fe-P/CNF) were also derived from BC via the pyrolysis of lyophilized $Fe[(HPO_4)_2]^-$ BC composite using $FeCl_3$ and H_3PO_4 as the doping sources.^[117] Using a fabrication process illustrated in Figure 8d, Fe-P/CNF catalyst exhibited significantly improved ORR onset potential (1.01 V vs RHE) and higher electron transfer number (3.9) than

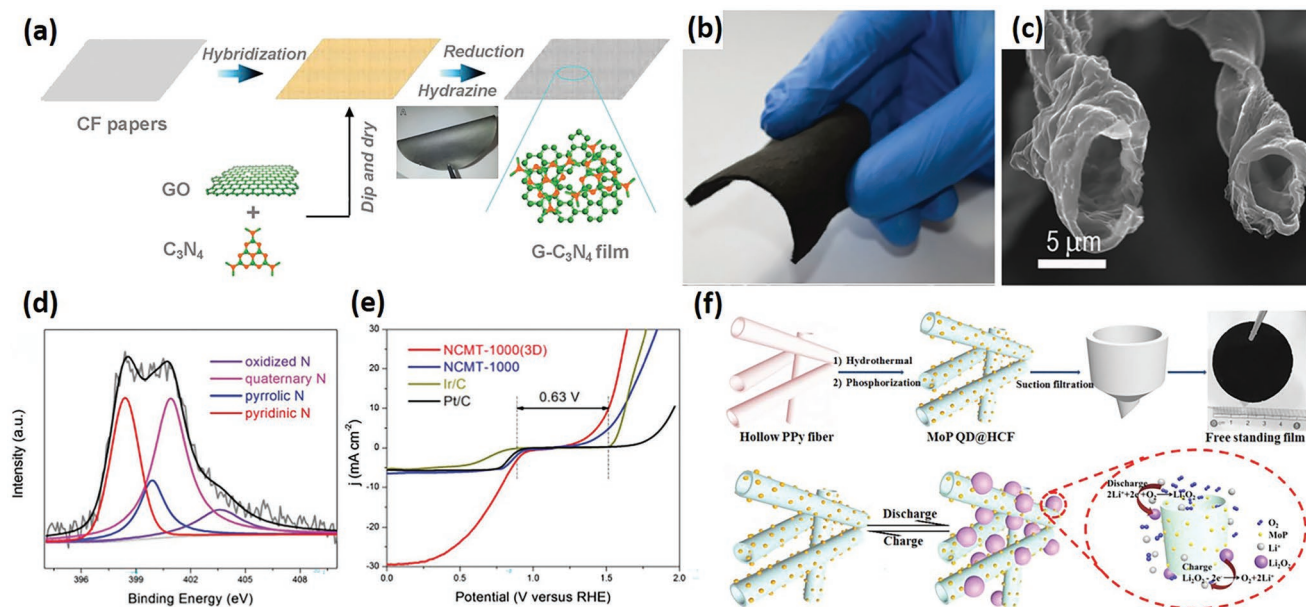


Figure 9. a) Schematic illustration of the fabrication of graphene and graphitic carbon nitrate (g-C₃N₄) on a cellulose fiber paper. Reproduced under the terms of the CC BY 4.0 license.^[125] Copyright 2015, The Authors, Published by WILEY-VCH Verlag GmbH & Co. KGaA, Weinheim. b) Optical and c) SEM image of N-doped carbon microtube (NCMT) sponge. Reproduced with permission.^[30] Copyright 2016, Royal Society of Chemistry. d) XPS spectra of N 1s of NCMT-1000. e) Oxygen electrode performance of NCMT-1000 (3D), NCMT-1000, Ir/C, and Pt/C in 0.1 M KOH. f) Schematic illustration of the fabrication of N, P-codoped hollow carbon fiber embedded with MoP quantum dots (MoP QD@HCF). Reproduced with permission.^[127] Copyright 2019, Elsevier.

P-doped or undoped CNFs (Figure 8e). The long-term stability was examined by the chronoamperometric method at a constant voltage of 0.6 V. The relative current density of Fe-P/CNFs remained 94% for 200 000 s, while only 64% sustained for the commercial 20 wt% Pt/C, demonstrating a superb long-term stability of Fe-P/CNFs.

3.3. Cellulose Fibrous Structures

Fibrous cellulose materials, mainly referring to fabrics and nonwovens, have a large number of functional groups (such as -OH and -OCO-) and 3D porous framework with large-scale availability and mature processability. Extensive research efforts have been made in transferring fibrous cellulose structures to freestanding carbon electrodes for foldable and flexible supercapacitors.^[120–123] As electrocatalytic electrodes, fibrous cellulose derived carbon structure have also been studied for hydrogen evolution reaction process.^[124]

Chen et al. fabricated a 3D N-doped carbon film by a facile “casting and drying” process of graphene and graphitic carbon nitrate (g-C₃N₄) ultrathin nanosheets on a cellulose fiber paper, followed by chemical reduction using hydrazine vapor to form a black film (Figure 9a), which achieved an OER onset potential of 387 mV.^[125]

Li et al. chose facial cotton pads as the raw material to prepare bifunctional ORR/OER catalyst.^[30] The experimental approach involved a pyrolysis procedure of cotton pad under NH₃ at 1000 °C to obtain N-doped carbon microtube (NCMT) (Figure 9b,c). It was found that the high contents of pyridinic and quaternary N in the NCMT sample (Figure 9d) played an

important role in achieving outstanding ORR performance. The 3D porous sponge exhibited an ORR potential of 0.89 V at a current density of -3 mA cm⁻², and an OER potential of 1.52 V at a current density of 10 mA cm⁻², much better than those of commercial electrocatalysts, as shown in Figure 9e. The chronoamperometry results showed that the current density decay of the NCMT-1000 catalyst (≈27%) was much smaller than that of Pt/C (≈50%) after 100 h of testing, showing improved durability.

Recently, another N-doped bifunctional catalyst was reported by Zhang et al. for water splitting.^[126] The cotton textile was first transformed into carbonized cloth in N₂, which was then dipped in PAN solution as a source of nitrogen, followed by a second carbonization process in N₂. This carbon cloth showed an OER overpotential of 351 mV at current density of 10 mA cm⁻².

3.4. Other Organic Materials

Other organic materials, such as aramid nanofibers and PPY fibers can also be used as the organic skeleton for synthesizing oxygen electrodes. Ren et al. developed a simple and effective approach for fabricating N-doped carbon nanofibers aerogels (NCNA) using commercial aramid fibers as the precursor.^[128] Solvent exchange process of aramid nanofibers solution and additional freeze-drying were employed to prepare aramid nanofiber aerogels. Finally, the NCNA were obtained through the pyrolysis of aramid nanofiber aerogels under nitrogen. The as-prepared NCNA exhibited excellent ORR performance in alkaline media, with a half-wave potential of 0.91 V, which was more positive than that of commercial Pt/C catalyst.

In addition, N, P-co-doped hollow carbon fiber embedded with MoP quantum dots was prepared by hydrothermal treatment of hollow PPy fibers with $(\text{NH}_4)_6\text{Mo}_7\text{O}_{24}$ and $\text{NH}_4\text{H}_2\text{PO}_4$, followed by a calcination process at 800°C with NaH_2PO_2 (Figure 9f).^[127] Because the open end structure of the hollow carbon fibers could serve as mass transfer channels and facilitate the electron transportation, the freestanding oxygen electrode delivered a higher discharge specific capacity of 6.75 mA h cm^{-2} and an enhanced rate capability up to 0.4 mA cm^{-2} .

4. Oxygen Electrocatalysts Supported on Carbon Cloth

In addition to the simultaneous formation of active catalytic sites and carbon matrix from organic fibrous structures, freestanding oxygen electrodes can also be fabricated using pre-existing conductive fibrous substrates. For example, commercially available CC can be an ideal candidate due to its

3D porous structure, excellent electrical conductivity, robust mechanical stability, and flexibility.

Because pristine carbon fibers in carbon cloth have very low electrochemical activity, direct surface treatments have been used to improve their electrocatalytic property. In an early work, OER performance of CC was greatly enhanced through oxidizing the CC with HNO_3 , with an onset potential only 66 mV more positive than RuO_2 catalyst.^[129] It was then found that both ORR and OER performance of CC could be considerably improved by Argon plasma treatment.^[130] By etching the amorphous carbon, edge/defect-rich graphene, and pore structures on fiber surface were produced, and further oxygen functionalization was conducted in air. It was demonstrated that the improvement of catalytic property was attributed to the edge carbon, O content, and structure defects. Wang et al. applied a H_2 etching approach to $\text{HCl}/\text{H}_2\text{O}_2$ oxidized CC, also leading to the formation of nanoporous carbon structure and defect-rich graphene skin.^[131] The electrochemical results showed that the OER and ORR current densities of modified carbon fiber were 20 and 3 times higher

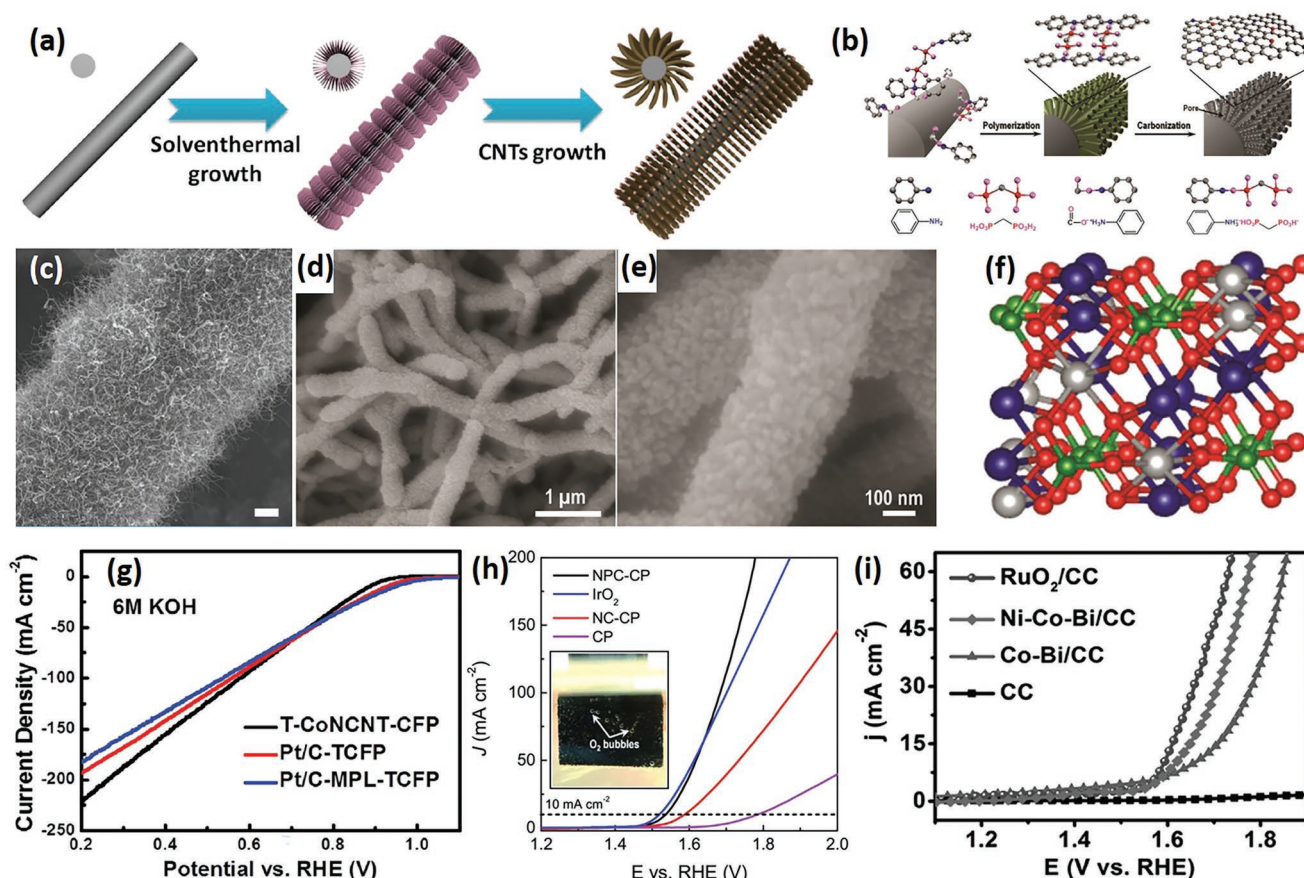


Figure 10. a) Schematic illustration of the fabrication of cobalt-incorporated nitrogen-doped carbon nanotube (CoNCNT) arrays on carbon fiber paper (CFP). Reproduced with permission.^[134] Copyright 2016, John Wiley and Sons. b) Schematic illustration of the fabrication of N and P-doped carbon nanofibers on carbon paper (NPC-CP). Reproduced with permission.^[135] Copyright 2017, John Wiley and Sons. c) SEM images of CoNCNTs on CFP. d) SEM images of NPC-CP. e) SEM images of Ni-Co-Bi nanowires on carbon cloth (Ni-Co-Bi/CC). Reproduced with permission.^[136] Copyright 2017, John Wiley and Sons. f) Structural diagrams of Ni-Co-Bi, blue, green, red, and silver spheres represent Co, B, O, and Ni atoms, respectively. g) ORR polarization curves of PTFE soaked CoNCNT-CFP in 6 M KOH, Pt/C catalyst on teflon-treated CFP (Pt/C-TCFP), and PTFE treated Pt/C-TCFP; h) OER polarization curves of NPC-CP, NC-CP, CP, and IrO₂ in 1 M KOH; i) OER polarization curves of Ni-Co-Bi/CC, Co-Bi/CC, CC, and RuO₂ on CC in 0.1 K-Bi.

Table 4. A summary of freestanding carbon cloth catalysts with active nanowires.

Material	Method	Electrolyte	Overpotential@10 [mV]	Tafel slope [mV dec ⁻¹]	Ref.
Fe ₂ O ₃ /CC	1. 120 °C hydrothermal treatment CC in FeCl ₃ + Na ₂ SO ₄ ; 2. Carbonization at 450 °C;	1 M KOH	420	52	[140]
NiCo ₂ O ₄ core-shell NW/CC	1. 110 °C hydrothermal treatment CC in Co(NO ₃) ₂ + Ni(NO ₃) ₂ + Co(NH ₂) ₂ ; 2. Air carbonization at 350 °C; 3. Electrodeposition in Co(NO ₃) ₂ + Ni(NO ₃) ₂ .	1 M KOH	320	63	[141]
Co ₄ N NW/CC	1. 120 °C hydrothermal treatment CC in Co(NO ₃) ₂ + NH ₄ F; 2. NH ₃ carbonization at 420 °C.	1 M KOH	257	44	[142]
NiD-PCC	1. 120 °C hydrothermal treatment CC in Ni(NO ₃) ₂ + Hexamethylene; 2. N ₂ Carbonization at 900 °C; 3. HCl etching for 12 h.	1 M KOH	360	98	[143]
CP@Ni-P	1. 60 °C oxidation of CC in H ₂ SO ₄ + HNO ₃ ; 2. Electrodeposition in NiSO ₄ + NiCl ₂ + H ₃ BO ₃ ; 3. 500 °C carbonization with red phosphorus in N ₂ .	1 M KOH	150	73	[144]
NiCo-LDH-NA	1. 180 °C hydrothermal treatment CC in Co(NO ₃) ₂ + Ni(NO ₃) ₂ + cetyltrimethylammonium bromide (CTAB).	1 M KOH	300	64	[37]
Cu(OH) ₂ @NiFe-LDH/CC	1. H ₂ SO ₄ washing; 2. Electrodeposition in Cu(NO ₃) ₂ to get Cu/CC; 3. Anodization in KOH to get Cu(OH) ₂ /CC; 4. Second electrodeposition in Ni(NO ₃) ₂ + FeSO ₄ .	1 M KOH	283	88	[145]
CuO@Co ₃ O ₄ core-shell NW/CC	1. H ₂ SO ₄ washing; 2. Electrodeposition in Cu(NO ₃) ₂ to get Cu/CC; 3. Anodization in KOH to get Cu(OH) ₂ /CC; 4. Second electrodeposition in Co(NO ₃) ₂ ; 5. 300 °C calcination.	1 M KOH	260	72	[146]
Co-ZnO/CF	1. 80 °C oxidation of CC in concentrated HNO ₃ ; 2. 180 °C hydrothermal treatment CC in Co(NO ₃) ₂ + Zn(NO ₃) ₂ + urea + NH ₄ F;	0.1 M KOH	360	68	[147]
Fe-Ni ₂ P/CC	1. 120 °C hydrothermal treatment CC in Ni(NO ₃) ₂ + Fe(NO ₃) ₃ + urea + NH ₄ F to get NiFe LDH/CC; 2. 300 °C carbonization of NiFe LDH/CC with NaH ₂ PO ₂ .	1 M KOH	190	48	[148]
Ni-Co-Bi/CC	1. 120 °C hydrothermal treatment CC in NiCl ₂ + CoCl ₂ + urea; 2. 450 °C annealing in air to get NiCo ₂ O ₄ /CC; 3. 400 °C carbonization with S powder in Ar to get NiCo ₂ S ₄ /CC; 4. Oxidative polarization with K-Bi to get Ni-Co-Bi/CC.	0.1 M K-Bi	390	142	[136]
Ni-Bi/CC	1. Preoxidization CC in concentrated HNO ₃ ; 2. 100 °C hydrothermal treatment in Ni(NO ₃) ₂ + hexamethylenetetramine (HMT) to get Ni(OH) ₂ /CC; 2. 300 °C annealing in Ar to get NiO/CC; 3. Oxidative polarization with K-Bi to get Ni-Bi/CC.	0.1 M K-Bi	470	107	[137]
NiO@Ni-Bi/CC	1. Preoxidization CC in concentrated HNO ₃ ; 2. 100 °C hydrothermal treatment in Ni(NO ₃) ₂ + HMT to get Ni(OH) ₂ /CC; 2. 350 °C annealing in air to get NiO/CC; 3. Oxidative polarization with K-Bi to get NiO@Ni-Bi/CC.	1 M KOH	290	71	[138]
NiCo ₂ O ₄ @Ni-Co-Ci core-shell NW/CC	1. 120 °C hydrothermal treatment CC in NiCl ₂ + CoCl ₂ + urea; 2. 450 °C annealing in air to get NiCo ₂ O ₄ /CC; 3. Oxidative polarization with K-Ci to get NiCo ₂ O ₄ @Ni-Co-Ci/CC.	1 M K-Ci	310	91	[139]
NiCo diselenide/CC	1. 180 °C hydrothermal treatment CC in Ni(NO ₃) ₂ + CoCl ₂ + CTAB + methanol to get NiCo hydroxide/CC; 2. 180 °C hydrothermal treatment of NiCo hydroxide/CC with NaHSe to get NiCo diselenide/CC	1 M KOH	258	42	[149]

Table 4. Continued.

Material	Method	Electrolyte	Overpotential@10 [mV]	Tafel slope [mV dec ⁻¹]	Ref.
Mn-Co-Bi/CC	1. Preoxidization CC in concentrated HNO ₃ ; 2. 120 °C hydrothermal treatment CC in Mn(NO ₃) ₂ + Co(NO ₃) ₂ + urea + NH ₄ F; 3. 300 °C annealing in air to get MnCo ₂ O ₄ /CC; 2. Oxidative polarization with K-Bi to get Mn-Co-Bi/CC.	0.5 M K-Bi	366	193	[150]
N-CoO/CC	1. 120 °C hydrothermal treatment CC in Co(NO ₃) ₂ + Co(NH ₂) ₂ + NH ₄ F to get Co ₂ (OH) ₂ CO ₃ NW/CC; 2. 550 °C annealing in Ar to get CoO NW/CC; 3. 300 °C annealing in NH ₃ to get N-doped CoO NW/CC	1 M KOH	319	74	[151]
N-WC/CC	1. 180 °C hydrothermal treatment CC in tungstic acid + H ₂ O ₂ + Na ₂ SO ₄ + HCl to get WO ₃ NW/CC. 2. 850 °C carbonization with melamine in Ar.	0.5 M H ₂ SO ₄	250	–	[152]
Mn-Ni-O/CC	1. Electropolymerization pyrrole monomers on CC in NaClO ₄ to get PPy@CC; 2. 160 °C hydrothermal treatment PPy@CC in phosphomolybdic acid + Ni(Ac) ₂ ; 3. 900 °C annealing in Ar to get Mo-Ni-O@CC.	1 M KOH	320	63	[153]
ONPPGC/OCC	1. Preoxidization CC in concentrated HNO ₃ ; 2. 160 °C hydrothermal treatment CC in aniline monomers + phytic acid + APS; 3. 1000 °C annealing in N ₂ .	0.5 M H ₂ SO ₄	430	84	[154]
NPC-CP	1. Preoxidization CC in concentrated HNO ₃ ; 2. Electropolymerization aniline monomers on CC in EDPA to get polyaniline hydrogel@CC; 3. 700 °C annealing in N ₂ .	1 M KOH	310	87	[135]

than those of pristine ones. In addition, Ma et al. introduced N and P dual dopants to CC under a heat treatment with melamine and ethylene diphosphonic acid, leading to the growth of P-doped g-C₃N₄ nanoflowers grown on carbon fiber paper.^[132] Before the treatment, CC was washed with HCl and oxidized with HNO₃, which was believed to create abundant carboxyl groups to interact with the active dopants. The obtained catalyst exhibited an ORR onset potential of 0.94 V and an OER overpotential of 400 mV at a current density of 10 mA cm⁻².

Except for improving electrocatalytic performance of carbon cloth itself, more recent researches have been performed to grow catalytic active materials on carbon fiber surface. Using PVP as the nitrogen source, Zhang et al. incorporated ultrafine transition metal nanoparticles (Ni-Fe, Ni-Mo) onto N-doped carbon cloth, which achieved an OER overpotential of 300 mV at current density of 10 mA cm⁻².^[133]

Figure 10a shows a typical example of using hydrothermal approach to construct Co(OH)₂ nanosheet arrays on CFP, followed by in situ growth of N-doped CNTs using melamine as the nitrogen and carbon sources at 600 °C (CoNCNT).^[134] Based on this synthetic process, Sun's group further developed metal-borate nanowires, e.g., Ni-Co-Bi, on carbon cloth via oxidative polarization of conventional nanoarrays in potassium borate (Ni-Co-Bi/CC).^[136–139] Recently, nitrogen and phosphorus codoped carbon nanofibers grown on CFP (NPC-CP) were prepared through an electrochemically induced polymerization approach in the presence of aniline monomer and phosphonic acid, as shown in **Figure 10b**.^[135]

Figure 10c–e, respectively, shows the SEM image of the catalysts prepared from these three methods. Sun et al. explained the intrinsic catalytic mechanism of Ni-Co-Bi/CC by building its structural diagram (**Figure 10f**).^[136] The density functional theory calculations suggested that the conversion of O* to OOH* was the rate-determining step and Ni substitution decreased the free energy of Co-Bi from 2.092 to 1.986 eV. It can be found from **Figure 10g–i** that these materials had close ORR or OER performance to commercially available catalysts.

Table 4 summarizes recently developed freestanding catalytic electrodes by growing different functional nanowires on carbon cloth surface, their fabrication method and electrocatalytic performance.

Recently, more attentions have been paid to using MOF as the precursor of functional materials. Dong et al. reported a MOF-derived Zn-doped CoSe₂ grown on carbon fabric as a freestanding OER catalyst.^[155] This kind of electrode exhibited an obviously enhanced OER activity in 1 M KOH aqueous solution compared with CoSe₂/CC, showing a small overpotential of 356 mV at a current density of 10 mA cm⁻² and an excellent stability.

Meng et al. combined electrodeposition and MOF growth to synthesize a bifunctional ORR/OER catalyst.^[156] As shown in **Figure 11a**, PPy nanofibers were first wrapped around carbon fibers using a three-electrode electrochemical approach. After loading Co-MOFs particles onto the PPy nanofiber layer on the carbon fibers, a freestanding electrode containing Co₄N, carbon fiber network, and carbon cloth (Co₄N/CNW/CC)

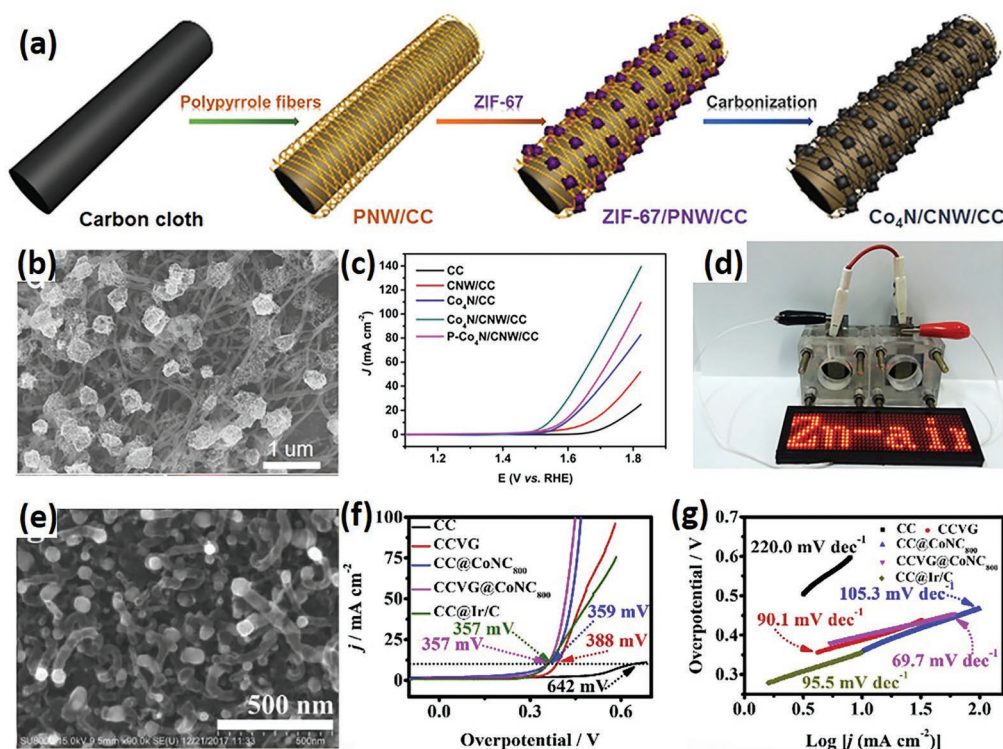


Figure 11. a) Schematic illustration of the fabrication of freestanding bifunctional electrode composed of Co_4N , carbon fiber network, and carbon cloth ($\text{Co}_4\text{N}/\text{CNW}/\text{CC}$). Reproduced with permission.^[156] Copyright 2016, American Chemical Society. b) SEM image of $\text{Co}_4\text{N}/\text{CNW}/\text{CC}$. c) OER polarization curves of $\text{Co}_4\text{N}/\text{CNW}/\text{CC}$ in 1 M KOH. d) Photograph of a small red LED powered by two Zn–air batteries with the $\text{Co}_4\text{N}/\text{CNW}/\text{CC}$ electrode connected in series. e) SEM image of $\text{CCVG}@\text{CoNC}$. Reproduced with permission.^[157] Copyright 2019, Elsevier. f) OER measurements of $\text{CCVG}@\text{CoNC}$ and benchmark electrocatalysts. g) Tafel plot curves of $\text{CCVG}@\text{CoNC}$.

was generated by an annealing process at 700 °C. Figure 11b shows the SEM images of the obtained catalyst. It can be seen that some Co_4N nanoparticles have penetrated into the porous carbon matrices. From the OER polarization curves in Figure 11c, the metallic Co_4N had superior OER activity with an overpotential of 310 mV. The freestanding catalyst was used to construct primary Zn–air batteries for demonstrating its feasibility in practical use (Figure 11d), and the initial discharge (1.16 V) and charge (2.00 V) voltages were well maintained even after continuous cycling of more than 136 h (up to 408 cycles).

More recently, vertically oriented graphene sheets were synthesized on CC (CCVG) by a plasma enhanced chemical vapor deposition method.^[158] After depositing Co-MOF particles onto this CCVG support, $\text{CCVG}@\text{CoNC}$ structure was obtained by a calcination process in Ar/H_2 atmosphere with melamine (Figure 11e).^[157] With an OER overpotential of 357 mV at 10 mA cm^{-2} and a Tafel slope of $\approx 70 \text{ mV dec}^{-1}$, this fibrous structure exhibited better performance than commercial RuO_2 (Figure 11f,g).

5. Oxygen Electrocatalysts Supported on Metal Substrates

Besides 2D metal foils, freestanding oxygen electrodes have also been fabricated by incorporating active species onto 3D

metal scaffolds, such as metal nanowire structures and metal meshes, which can enhance electrocatalytic activity by providing high electrical conductivity, high catalyst loading, smooth mass transfer, and stable electrical connection.

5.1. Te Nanowires

Yu's group prepared $\text{Te}@\text{C}$ nanocables through hydrothermal treatment of a mixture of Te nanowires and glucose. By adding H_2PtCl_6 into the $\text{Te}@\text{C}$ nanocable suspension, freestanding Pt nanowire membrane was obtained after suspension casting and calcination treatment, as shown in Figure 12a. The Pt nanowire membrane displayed more positive onset potential than Pt black, and comparable mass activity with Pt/C catalysts during an ORR test at 0.85 V.^[159] In another study, pyrrole and Fe^{3+} were incorporated into the lyophilized $\text{Te}@\text{C}$ nanocables, followed by a carbonization in N_2 and acid leaching treatment, resulting in mesoporous Fe-N-doped carbon nanofibers.^[160] The catalyst exhibited outstanding ORR activity with an onset potential of 0.95 V, which was very close to that of Pt/C catalyst. Using a simple three-electrode electrodeposition approach, another transition metal catalyst Co-S/Ti mesh was reported with encouraging OER performance of 360 mV overpotential at 10 mA cm^{-2} .^[161]

Using glucosamine hydrochloride and thiourea as the nitrogen and sulfur sources, a N/S co-doped Te nanowire

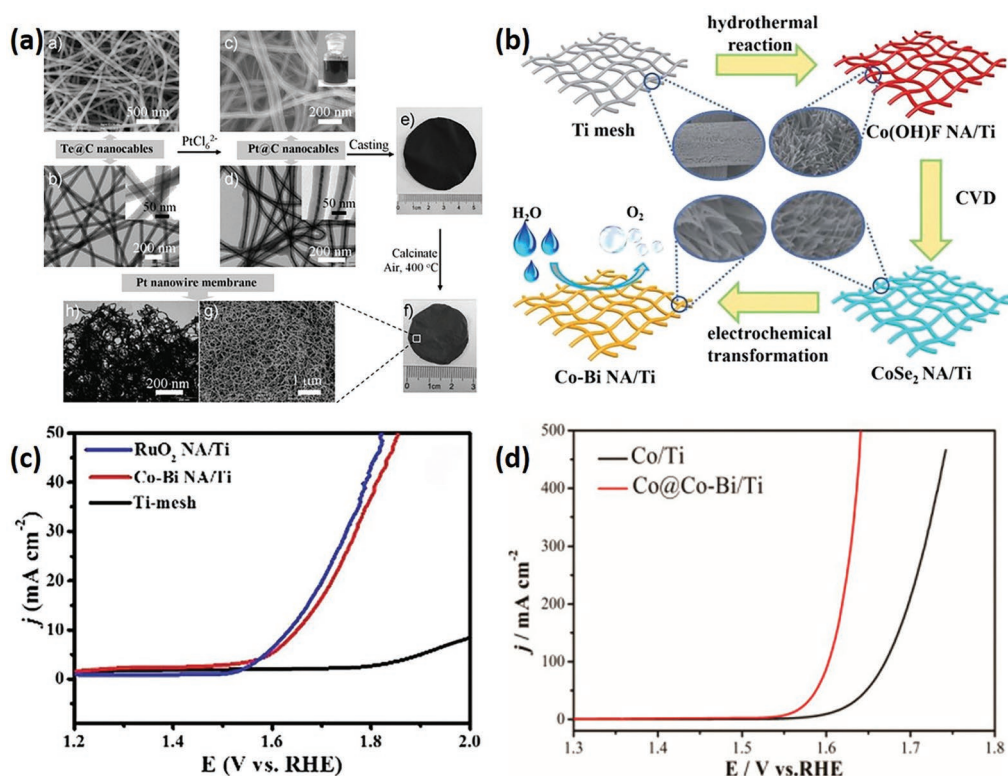


Figure 12. a) Schematic illustration of the fabrication of freestanding Pt nanowires membrane. Reproduced with permission.^[159] Copyright 2011, John Wiley and Sons. b) Schematic illustration of the fabrication of Co-Bi nanowires on Ti mesh (Co-Bi NA/Ti). Reproduced with permission.^[163] Copyright 2017, Royal Society of Chemistry. c,d) OER LSV curves of Co-Bi NA/Ti in 0.1 M K-Bi and Co@Co-Bi/Ti in 1 M KOH. Reproduced with permission.^[166] Copyright 2017, Royal Society of Chemistry.

aerogel was synthesized by the combination of hydrothermal treatment and carbonization.^[162] Upon adjusting the N/S mass ratio, the optimized metal-free aerogel showed an onset potential and half-wave potential of 0.905 and 0.838 V, comparable to those of commercial Pt/C (0.931 and 0.851 V), but with better methanol tolerance and stability.

5.2. Metal Mesh

It can be found from Table 2 that a large amount of work has been conducted to stabilize metal nanowires on carbon cloth. At the same time, metal mesh can also serve as a robust support for the growth of functional nanostructures. One of the techniques applied to synthesize metal (such as Ni and Co) selenides nanowires was hydrothermal treatment of the mixture of metal nitrates, NH_4F and urea, followed by a heat treatment with selenium powders. The other method was through electrodeposition in metal nitrates solution to prepare metal hydroxides nanoarrays on a Ti mesh ($\text{Co(OH)}_2/\text{Ti}$). Finally, these nanowires were converted to metal-borate species in potassium borate (K-Bi) via an in situ electrochemical treatment (Figure 12b),^[163–165] in which the Co-Bi/Ti showed an OER overpotential of 420 mV at current density of 10 mA cm^{-2} in 0.1 M K-Bi solution (Figure 12c).^[163] In addition, Co@Co-Bi nanosheets on Ti-mesh (Co@Co-Bi/Ti) were synthesized via a two-step method of electrochemical deposition, and OER LSV

curves in Figure 12d reveals its high OER activity with a relatively small overpotential of 329 mV to obtain a current density of 10 mA cm^{-2} in an alkaline solution.^[166]

Cai et al. reported the fabrication of metal oxide@MOF-derived porous carbon hybrid arrays on Cu mesh and Fe mesh. CoO nanorods were hydrothermally grown on Cu mesh and Fe mesh (Cu/Fe Mesh@CoO) with cobalt nitrate, NH_4F , and urea, followed by a 350 °C annealing in N_2 . Then Co-ZIF particles were in situ grown onto the meshes to obtain Cu Mesh@CoO@ZIF-67 and Fe Mesh@CoO@ZIF-67 by immersing the obtained meshes into the MOF precursor solution. Through simple pyrolysis, this kind of free-standing catalyst could be directly used for water splitting.^[169]

Stainless steel (SS) mesh can also serve as current collector and catalyst support.^[170,171] Through a pretreatment in a solution containing $\text{Co(NO}_3)_2$, NH_4NO_3 , and NH_4OH at 90 °C for 12 h, Co_3O_4 nanowires were generated on a SS mesh current collector after an air carbonization at 300 °C (Figure 13a). The Co_3O_4 nanowire had an average diameter and length of 300 nm and 15 μm , as shown in Figure 13b. The bare SS mesh was fully covered with Co_3O_4 NW after the growth (Figure 13c,d), creating a 3D binder-free electrode. Using this electrode in a rechargeable Zn–air battery, superior discharge and charge potentials were obtained (Figure 13e). Moreover, the cycling charge and discharge potential retained 97% and 94%, respectively, after 600 h testing, demonstrating remarkable durability of this advanced electrode.^[167]

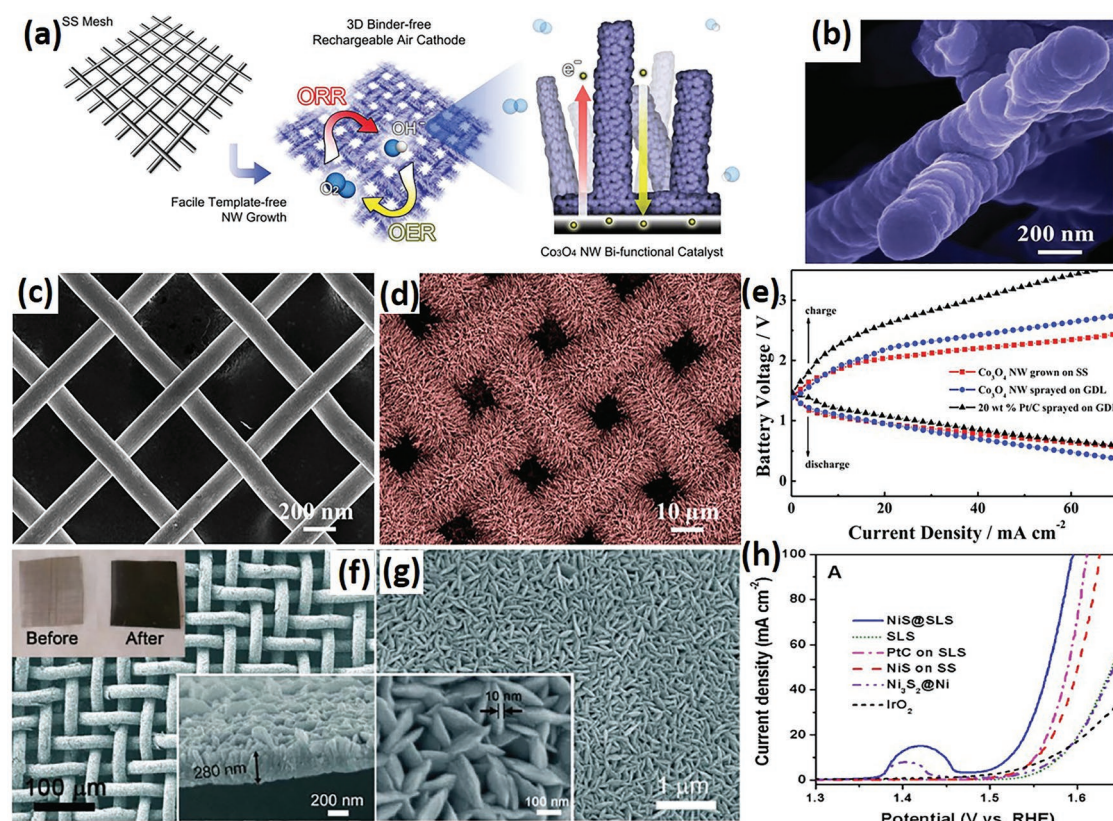


Figure 13. a) Schematic illustration of the fabrication and b) optical image of 3D rechargeable Co₃O₄ nanowires air cathode. Reproduced with permission.^[167] Copyright 2013, John Wiley and Sons. SEM image of SS mesh current collector c) before and d) after Co₃O₄ nanowires growth. e) Galvanodynamic discharge-charge polarization curves of Co₃O₄ nanowires grown on SS mesh, Co₃O₄ nanowires sprayed on a carbon gas diffusion layer (GDL) and Pt/C on GDL. f, g) SEM images of the NiS nanosheets grown on SS mesh (NiS@SS). Reproduced with permission.^[168] Copyright 2016, American Chemical Society. h) OER LSV curves of NiS@SS and other catalysts.

Ni-modified CoOOH nanowires were synthesized on SS meshes using a chemical deposition technique followed by chemical oxidation in H₂O₂. The OER activity of Ni-CoOOH reached a maximum value at a Ni content of 9.7%, demonstrating that the modification of Ni on CoOOH nanowires created more active sites for OER process.^[172] A freestanding nickel sulfide (NiS) nanosheet array was grown on an SS mesh via a one-pot hydrothermal method. It can be found from Figure 13f that the mesh structure was maintained after the hydrothermal treatment, and the color of the SS mesh changed from silvery white to black, suggesting the successful deposition of a uniform NiS layer. The SS wire surface was completely covered by with vertically aligned sheet-like structures with a thickness of about 10 nm and a sheet size of ≈200 nm (Figure 13g). The NiS@SS mesh electrode exhibited a low overpotential of 290 mV at a current density of 10 mA cm⁻² (Figure 13h).^[168]

6. Summary and Outlook

Exploiting efficient and durable ORR/OER catalysts is of crucial importance in the development of many energy devices involving oxygen electrochemical reactions, such as fuel cells, metal-air batteries, and water splitting units. Compared

with conventional electrodes fabricated using powdery catalyst pastes, freestanding oxygen electrodes integrating in situ grown active catalytic materials have the advantages of simple electrode preparation, decreased interface resistance, reduced particle agglomeration, enhanced stability, improved mass transfer, and promising catalytic performance. Among all available freestanding structures, fibrous materials have exhibited many unique characteristics, such as a wide range of fiber selection, low material source and processing costs, large specific surface area, highly porous structure, and simplicity of fiber functionalization.

In this article, we have summarized the latest development of freestanding electrodes for oxygen electrocatalysis using different fibrous structures, from organic fibrous sources (such as electrospun nanofibers, bacterial cellulose, and cellulose fibrous structures) to conductive fibrous substrates (such as carbon clothes/fabrics, metal nanowires, and metal meshes). It has been found that by incorporating functional materials, such as non-noble metals, heteroatom doping, and MOFs, with various types of fibers, fibrous-structured freestanding oxygen electrodes can exhibit promising electrocatalytic performance.

Future development of practically applicable oxygen electrodes for energy devices requires more research efforts to tackle some scientific and technical challenges.

First, more systematic investigations are required to achieve fundamental understanding of the effects of fiber dimension, morphology, surface roughness, and fibrous structure on electrode performance.

Second, majority of previous work only focused on a single oxygen reaction, while bifunctional ORR/OER electrodes are more desirable for practical device application. More attentions need to be paid to the development of bifunctional free-standing oxygen electrodes. In addition, most of the oxygen electrocatalysts developed so far only function under alkaline conditions. Upon understanding the different electrochemistry in acid media, it would be favorable to exploit bifunctional fibrous ORR/OER electrodes that can efficiently work at all pH values.

Third, more cost-effective and environmentally friendly synthetic methods should be developed. Currently, most of reported studies involved expensive carbon precursors and corrosive or highly dangerous gas like NH_3 or H_2 , which imposes great pressure on the environment.

Fourth, currently reported electrochemical results of free-standing electrode are not always comparable since some were based on the weight of entire electrode and many others only considered the content of active catalytic material. Therefore, a reliable procedure should be developed to comparably evaluate the electrocatalytic properties of these electrodes.

Finally, many freestanding oxygen electrodes were characterized by the approach previously developed for powdery catalysts, which may not be able to present their full catalytic capacity. Especially during device fabrication, the direct use of freestanding structures as oxygen electrode requires more studies to understand their practical performance in different device structures and electrolyte conditions.

With continuous research efforts in this area, it can be optimizely expected that fibrous structure will make more important contribution to the development of freestanding electrodes for the advanced energy devices involving oxygen electrochemistry.

Acknowledgements

The authors would like to thank the support from Australian Research Council (ARC) through ARC Centre of Excellence for Electromaterials Science (ACES) (No. CE140100012). This work was also supported by the Australian Research Council World Class Future Fibre Industry Transformation Research Hub (No. IH140100018).

Conflict of Interest

The authors declare no conflict of interest.

Keywords

electrocatalysis, fibrous structures, freestanding electrodes, oxygen electrodes

Received: July 15, 2019
Revised: September 2, 2019
Published online:

- [1] A. S. Aricò, P. Bruce, B. Scrosati, J. M. Tarascon, W. Van Schalkwijk, *Nat. Mater.* **2005**, *4*, 366.
- [2] I. Katsounaros, S. Cherevko, A. R. Zeradjanin, K. J. Mayrhofer, *Angew. Chem., Int. Ed.* **2014**, *53*, 102.
- [3] Y. Jiao, Y. Zheng, M. Jaroniec, S. Z. Qiao, *Chem. Soc. Rev.* **2015**, *44*, 2060.
- [4] C. R. Raj, A. Samanta, S. H. Noh, S. Mondal, T. Okajima, T. Ohsaka, *J. Mater. Chem. A* **2016**, *4*, 11156.
- [5] F. Cheng, J. Chen, *Chem. Soc. Rev.* **2012**, *41*, 2172.
- [6] A. Sarapu, E. Kibena Pöldsepp, M. Borghei, K. Tammeveski, *J. Mater. Chem. A* **2018**, *6*, 776.
- [7] Z. Chen, D. Higgins, A. Yu, L. Zhang, J. Zhang, *Energy Environ. Sci.* **2011**, *4*, 3167.
- [8] N. T. Suen, S. F. Hung, Q. Quan, N. Zhang, Y. J. Xu, H. M. Chen, *Chem. Soc. Rev.* **2017**, *46*, 337.
- [9] Z. Huang, J. Wang, Y. Peng, C. Jung, A. Fisher, X. Wang, *Adv. Energy Mater.* **2017**, *7*, 1700544.
- [10] J. Liu, D. Zhu, Y. Zheng, A. Vasileff, S. Z. Qiao, *ACS Catal.* **2018**, *8*, 6707.
- [11] T. Y. Ma, S. Dai, S. Z. Qiao, *Mater. Today* **2016**, *19*, 265.
- [12] J. Lai, A. Nsabimana, R. Luque, G. Xu, *Joule* **2018**, *2*, 76.
- [13] T. Jin, Q. Han, L. Jiao, *Adv. Mater.* **2019**, *31*, 1806304.
- [14] H. Sun, Z. Yan, F. Liu, W. Xu, F. Cheng, J. Chen, *Adv. Mater.* **2019**, *31*, 1806326.
- [15] G. Yuan, X. Niu, Z. Chen, L. Wang, X. Zhang, Q. Wang, *ChemElectroChem* **2018**, *5*, 2376.
- [16] S. H. Yu, W. Chen, H. Wang, H. Pan, D. H. Chua, *Nano Energy* **2019**, *55*, 193.
- [17] X. Lv, Z. Hu, J. Ren, Y. Liu, Z. Wang, Z. Y. Yuan, *Inorg. Chem. Front.* **2019**, *6*, 74.
- [18] Y. Yang, J. Wang, Y. Zhu, L. Lan, H. Zhang, C. Liu, K. Tao, J. Li, *Int. J. Hydrogen Energy* **2019**, *44*, 19672.
- [19] J. Hu, Z. Shi, X. Wang, H. Qiao, H. Huang, *Electrochim. Acta* **2019**, *302*, 216.
- [20] T. C. Hsieh, Y. H. Tsou, J. S. Chen, *Electrochim. Acta* **2019**, *295*, 490.
- [21] J. Liang, G. Zhu, C. Wang, Y. Wang, H. Zhu, Y. Hu, H. Lv, R. Chen, L. Ma, T. Chen, *Adv. Energy Mater.* **2017**, *7*, 1601208.
- [22] H. F. Wang, R. Chen, J. Feng, M. Qiao, S. Doszdeczko, Q. Zhang, A. B. Jorge, M. M. Titirici, *ChemElectroChem* **2018**, *5*, 1786.
- [23] J. Zhang, *PEM Fuel Cell Electrocatalysts and Catalyst Layers: Fundamentals and Applications*, Springer Science & Business Media, London **2008**.
- [24] L. Yu, X. Pan, X. Cao, P. Hu, X. Bao, *J. Catal.* **2011**, *282*, 183.
- [25] J. K. Nørskov, J. Rossmeisl, A. Logadottir, L. Lindqvist, J. R. Kitchin, T. Bligaard, H. Jonsson, *J. Phys. Chem. B* **2004**, *108*, 17886.
- [26] Z. W. Seh, J. Kibsgaard, C. F. Dickens, I. Chorkendorff, J. K. Nørskov, T. F. Jaramillo, *Science* **2017**, *355*, eaad4998.
- [27] H. Yan, B. Xu, S. Shi, C. Ouyang, *J. Appl. Phys.* **2012**, *112*, 104316.
- [28] M. Tahir, L. Pan, F. Idrees, X. Zhang, L. Wang, J. J. Zou, Z. L. Wang, *Nano Energy* **2017**, *37*, 136.
- [29] Q. Xue, Y. Ding, Y. Xue, F. Li, P. Chen, Y. Chen, *Carbon* **2018**, *139*, 137.
- [30] J. Li, P. Hou, S. Zhao, C. Liu, D. Tang, M. Cheng, F. Zhang, H. Cheng, *Energy Environ. Sci.* **2016**, *9*, 3079.
- [31] D. Liu, X. Zhang, Z. Sun, T. You, *Nanoscale* **2013**, *5*, 9528.
- [32] M. S. Balogun, W. Qiu, H. Yang, W. Fan, Y. Huang, P. Fang, G. Li, H. Ji, Y. Tong, *Energy Environ. Sci.* **2016**, *9*, 3411.
- [33] F. Jing, Q. Lv, J. Xiao, Q. Wang, S. Wang, *J. Mater. Chem. A* **2018**, *6*, 14207.
- [34] Y. Wu, Y. Gao, H. He, P. Zhang, *Electrochim. Acta* **2019**, *301*, 39.
- [35] H. B. Yang, J. Miao, S.-F. Hung, J. Chen, H. B. Tao, X. Wang, L. Zhang, R. Chen, J. Gao, H. M. Chen, *Sci. Adv.* **2016**, *2*, e1501122.
- [36] C. Wei, S. Sun, D. Mandler, X. Wang, S. Z. Qiao, Z. J. Xu, *Chem. Soc. Rev.* **2019**, *48*, 2518.

- [37] C. Yu, Z. Liu, X. Han, H. Huang, C. Zhao, J. Yang, J. Qiu, *Carbon* **2016**, 110, 1.
- [38] Y. Yang, L. Dang, M. J. Shearer, H. Sheng, W. Li, J. Chen, P. Xiao, Y. Zhang, R. J. Hamers, S. Jin, *Adv. Energy Mater.* **2018**, 8, 1703189.
- [39] B. Wang, X. Wang, J. Zou, Y. Yan, S. Xie, G. Hu, Y. Li, A. Dong, *Nano Lett.* **2017**, 17, 2003.
- [40] W. Wang, Y. Liu, J. Li, J. Luo, L. Fu, S. Chen, *J. Mater. Chem. A* **2018**, 6, 14299.
- [41] B. Chen, X. He, F. Yin, H. Wang, D. J. Liu, R. Shi, J. Chen, H. Yin, *Adv. Funct. Mater.* **2017**, 27, 1700795.
- [42] Q. Wang, Y. Lei, Z. Chen, N. Wu, Y. Wang, B. Wang, Y. Wang, *J. Mater. Chem. A* **2018**, 6, 516.
- [43] C. Y. Su, H. Cheng, W. Li, Z. Q. Liu, N. Li, Z. Hou, F. Q. Bai, H. X. Zhang, T. Y. Ma, *Adv. Energy Mater.* **2017**, 7, 1602420.
- [44] S. Peng, X. Han, L. Li, S. Chou, D. Ji, H. Huang, Y. Du, J. Liu, S. Ramakrishna, *Adv. Energy Mater.* **2018**, 8, 1800612.
- [45] Q. Liu, Y. Wang, L. Dai, J. Yao, *Adv. Mater.* **2016**, 28, 3000.
- [46] M. J. Tan, B. Li, P. Chee, X. Ge, Z. Liu, Y. Zong, X. J. Loh, *J. Power Sources* **2018**, 400, 566.
- [47] Z. Pei, Y. Huang, Z. Tang, L. Ma, Z. Liu, Q. Xue, Z. Wang, H. Li, Y. Chen, C. Zhi, *Energy Storage Mater.* **2018**, 20, 234.
- [48] G. Wu, S. Lin, C. Yang, *J. Membr. Sci.* **2006**, 280, 802.
- [49] Z. Lin, L. Ji, O. Toprakci, W. Krause, X. Zhang, *J. Mater. Res.* **2010**, 25, 1329.
- [50] Y. Qiu, J. Yu, T. Shi, X. Zhou, X. Bai, J. Y. Huang, *J. Power Sources* **2011**, 196, 9862.
- [51] J. Yin, Y. Qiu, J. Yu, X. Zhou, W. Wu, *RSC Adv.* **2013**, 3, 15655.
- [52] S. Wang, C. Dai, J. Li, L. Zhao, Z. Ren, Y. Ren, Y. Qiu, J. Yu, *Int. J. Hydrogen Energy* **2015**, 40, 4673.
- [53] A. Jindal, D. K. Gautam, S. Basu, *J. Electroanal. Chem.* **2016**, 775, 198.
- [54] Y. Chen, Q. Liu, J. Wang, *Nano Adv.* **2016**, 1, 79.
- [55] R. Jasinski, *Nature* **1964**, 201, 1212.
- [56] Y. Zhao, J. Zhang, X. Guo, H. Fan, W. Wu, H. Liu, G. Wang, *J. Mater. Chem. A* **2017**, 5, 19672.
- [57] Y. Li, S. Chen, D. Xi, Y. Bo, R. Long, C. Wang, L. Song, Y. Xiong, *Small* **2018**, 14, 1702109.
- [58] X. Wang, Y. Li, T. Jin, J. Meng, L. Jiao, M. Zhu, J. Chen, *Nano Lett.* **2017**, 17, 7989.
- [59] J. Yin, Y. Qiu, J. Yu, *Electrochim. Commun.* **2013**, 30, 1.
- [60] D. Shin, B. Jeong, B. S. Mun, H. Jeon, H. J. Shin, J. Baik, J. Lee, *J. Phys. Chem. C* **2013**, 117, 11619.
- [61] Y. Qiu, J. Yu, W. Wu, J. Yin, X. Bai, *J. Solid State Electrochem.* **2013**, 17, 565.
- [62] Q. Guo, D. Zhao, S. Liu, S. Chen, M. Hanif, H. Hou, *Electrochim. Acta* **2014**, 138, 318.
- [63] P. Zamani, D. Higgins, F. Hassan, G. Jiang, J. Wu, S. Abureden, Z. Chen, *Electrochim. Acta* **2014**, 139, 111.
- [64] D. Shin, X. An, M. Choun, J. Lee, *Catal. Today* **2016**, 260, 82.
- [65] X. Yan, L. Gan, Y. C. Lin, L. Bai, T. Wang, X. Wang, J. Luo, J. Zhu, *Small* **2014**, 10, 4072.
- [66] X. Yan, K. Liu, X. Wang, T. Wang, J. Luo, J. Zhu, *Nanotechnology* **2015**, 26, 165401.
- [67] C. Shang, M. Li, Z. Wang, S. Wu, Z. Lu, *ChemElectroChem* **2016**, 3, 1437.
- [68] N. Wu, Y. Wang, Y. Lei, B. Wang, C. Han, Y. Gou, Q. Shi, D. Fang, *Sci. Rep.* **2015**, 5, 17396.
- [69] S. Wang, Z. Cui, M. Cao, *Chem. – Eur. J.* **2015**, 21, 2165.
- [70] Y. W. Ju, S. Yoo, C. Kim, S. Kim, I. Y. Jeon, J. Shin, J. B. Baek, G. Kim, *Adv. Sci.* **2016**, 3, 1500205.
- [71] B. Li, S. P. Sasikala, D. H. Kim, J. Bak, I. D. Kim, E. Cho, S. O. Kim, *Nano Energy* **2019**, 56, 524.
- [72] Q. Shi, Y. Lei, Y. Wang, H. Wang, L. Jiang, H. Yuan, D. Fang, B. Wang, N. Wu, Y. Gou, *Curr. Appl. Phys.* **2015**, 15, 1606.
- [73] J. Guo, Q. Niu, Y. Yuan, I. Maitlo, J. Nie, G. Ma, *Appl. Surf. Sci.* **2017**, 416, 118.
- [74] B. Li, X. Ge, F. T. Goh, D. Geng, G. Du, Z. Liu, J. Zhang, X. Liu, Y. Zong, *Nanoscale* **2015**, 7, 1830.
- [75] C. Alegre, C. Busacca, O. Di Blasi, V. Antonucci, A. S. Aricò, A. Di Blasi, V. Baglio, *J. Power Sources* **2017**, 364, 101.
- [76] Y. Wang, J. Fu, Y. Zhang, M. Li, F. M. Hassan, G. Li, Z. Chen, *Nanoscale* **2017**, 9, 15865.
- [77] S. Surendran, S. Shanmugapriya, A. Sivanantham, S. Shanmugam, R. Kalai Selvan, *Adv. Energy Mater.* **2018**, 8, 1800555.
- [78] C. Liu, J. Wang, J. Li, J. Liu, C. Wang, X. Sun, J. Shen, W. Han, L. Wang, *J. Mater. Chem. A* **2017**, 5, 1211.
- [79] Q. Niu, J. Guo, B. Chen, J. Nie, X. Guo, G. Ma, *Carbon* **2017**, 114, 250.
- [80] D. Ji, L. Fan, L. Li, S. Peng, D. Yu, J. Song, S. Ramakrishna, S. Guo, *Adv. Mater.* **2019**, 31, 1808267.
- [81] D. Ji, S. Peng, L. Fan, L. Li, X. Qin, S. Ramakrishna, *J. Mater. Chem. A* **2017**, 5, 23898.
- [82] Z. Chen, M. Waje, W. Li, Y. Yan, *Angew. Chem., Int. Ed.* **2007**, 46, 4060.
- [83] H. J. Kim, Y. S. Kim, M. H. Seo, S. M. Choi, J. Cho, G. W. Huber, W. B. Kim, *Electrochim. Commun.* **2010**, 12, 32.
- [84] J.-I. Shui, C. Chen, J. C. Li, *Adv. Funct. Mater.* **2011**, 21, 3357.
- [85] X. Zhou, Y. Qiu, J. Yu, J. Yin, S. Gao, *Int. J. Hydrogen Energy* **2011**, 36, 7398.
- [86] A. Yu, C. Lee, N. S. Lee, M. H. Kim, Y. Lee, *ACS Appl. Mater. Interfaces* **2016**, 8, 32833.
- [87] J. Lee, C. Jo, B. Park, W. Hwang, H. I. Lee, S. Yoon, J. Lee, *Nanoscale* **2014**, 6, 10147.
- [88] M. Li, Y. Xiong, X. Liu, X. Bo, Y. Zhang, C. Han, L. Guo, *Nanoscale* **2015**, 7, 8920.
- [89] P. Li, J. Zhang, Q. Yu, J. Qiao, Z. Wang, D. Rooney, W. Sun, K. Sun, *Electrochim. Acta* **2015**, 165, 78.
- [90] K. R. Yoon, G. Y. Lee, J. W. Jung, N. H. Kim, S. O. Kim, I. D. Kim, *Nano Lett.* **2016**, 16, 2076.
- [91] V. D. Silva, T. A. Simões, F. J. Loureiro, D. P. Fagg, F. M. Figueiredo, E. S. Medeiros, D. A. Macedo, *Int. J. Hydrogen Energy* **2019**, 44, 14877.
- [92] V. D. Silva, T. A. Simões, F. J. Loureiro, D. P. Fagg, E. S. Medeiros, D. A. Macedo, *Mater. Lett.* **2018**, 221, 81.
- [93] V. D. Silva, L. S. Ferreira, T. A. Simões, E. S. Medeiros, D. A. Macedo, *J. Colloid Interface Sci.* **2019**, 540, 59.
- [94] H. Chen, X. Huang, L. Zhou, G. Li, M. Fan, X. Zou, *ChemCatChem* **2016**, 8, 992.
- [95] T. Li, Y. Lv, J. Su, Y. Wang, Q. Yang, Y. Zhang, J. Zhou, L. Xu, D. Sun, Y. Tang, *Adv. Sci.* **2017**, 4, 1700226.
- [96] Y. E. Miao, F. Li, H. Lu, J. Yan, Y. Huang, T. Liu, *Compos. Commun.* **2016**, 1, 15.
- [97] G. Ren, X. Lu, Y. Li, Y. Zhu, L. Dai, L. Jiang, *ACS Appl. Mater. Interfaces* **2016**, 8, 4118.
- [98] B. Patil, B. Satilmis, M. A. Khalily, T. Uyar, *ChemSusChem* **2019**, 12, 1469.
- [99] Y. Wang, J. Jin, S. Yang, G. Li, J. Jiang, *Int. J. Hydrogen Energy* **2016**, 41, 11174.
- [100] C. Lai, P. Kolla, Y. Zhao, H. Fong, A. L. Smirnova, *Electrochim. Acta* **2014**, 130, 431.
- [101] D. Zhen, B. Zhao, H. C. Shin, Y. Bu, Y. Ding, G. He, M. Liu, *Adv. Mater. Interfaces* **2017**, 4, 1700146.
- [102] Y. Fu, H. Y. Yu, C. Jiang, T.-H. Zhang, R. Zhan, X. Li, J.-F. Li, J.-H. Tian, R. Yang, *Adv. Funct. Mater.* **2018**, 28, 1705094.
- [103] G. S. Park, J. S. Lee, S. T. Kim, S. Park, J. Cho, *J. Power Sources* **2013**, 243, 267.
- [104] Y. Qiu, J. Yin, H. Hou, J. Yu, X. Zuo, *Electrochim. Acta* **2013**, 96, 225.

- [105] J. Yin, Y. Qiu, J. Yu, *J. Electroanal. Chem.* **2013**, 702, 56.
- [106] Y. Cao, H. Lu, Q. Hong, B. Xu, J. Wang, Y. Deng, W. Yang, W. Cai, *Carbon* **2019**, 144, 280.
- [107] D. Ji, S. Peng, J. Lu, L. Li, S. Yang, G. Yang, X. Qin, M. Srinivasan, S. Ramakrishna, *J. Mater. Chem. A* **2017**, 5, 7507.
- [108] B. Kim, Y. Choi, S. Y. Cho, Y. S. Yun, H. J. Jin, *J. Nanosci. Nanotechnol.* **2013**, 13, 7454.
- [109] T. Zhang, Y. Zheng, S. Liu, L. Yue, Y. Gao, Y. Yao, *J. Electroanal. Chem.* **2015**, 750, 43.
- [110] Y. Huang, T. Wang, M. Ji, J. Yang, C. Zhu, D. Sun, *Mater. Lett.* **2014**, 128, 93.
- [111] F. Meng, L. Li, Z. Wu, H. Zhong, J. Li, J. Yan, *Chin. J. Catal.* **2014**, 35, 877.
- [112] H. Liang, Z. Wu, L. Chen, C. Li, S. Yu, *Nano Energy* **2015**, 11, 366.
- [113] T. Ye, L. Lv, X. Li, M. Xu, J. Chen, *Angew. Chem., Int. Ed.* **2014**, 53, 6905.
- [114] R. Li, X. Shao, S. Li, P. Cheng, Z. Hu, D. Yuan, *Nanotechnology* **2016**, 27, 505402.
- [115] J. Liu, Y. G. Ji, B. Qiao, F. Zhao, H. Gao, P. Chen, Z. An, X. Chen, Y. Chen, *Catalysts* **2018**, 8, 269.
- [116] G. Cao, Y. Yan, T. Liu, D. Rooney, Y. Guo, K. Sun, *Carbon* **2015**, 94, 680.
- [117] S. Li, W. Xu, P. Cheng, J. Luo, D. Zhou, J. Li, R. Li, D. Yuan, *Synth. Met.* **2017**, 223, 137.
- [118] T. Liu, Y. Guo, Y. Yan, F. Wang, C. Deng, D. Rooney, K. Sun, *Carbon* **2016**, 106, 84.
- [119] S. Liu, W. Yan, X. Cao, Z. Zhou, R. Yang, *Int. J. Hydrogen Energy* **2016**, 41, 5351.
- [120] L. Chen, T. Ji, L. Mu, J. Zhu, *Carbon* **2017**, 111, 839.
- [121] L. Liu, Z. Niu, L. Zhang, W. Zhou, X. Chen, S. Xie, *Adv. Mater.* **2014**, 26, 4855.
- [122] J. Xue, Y. Zhao, H. Cheng, C. Hu, Y. Hu, Y. Meng, H. Shao, Z. Zhang, L. Qu, *Phys. Chem. Chem. Phys.* **2013**, 15, 8042.
- [123] L. Li, Q. Zhong, N. D. Kim, G. Ruan, Y. Yang, C. Gao, H. Fei, Y. Li, Y. Ji, J. M. Tour, *Carbon* **2016**, 105, 260.
- [124] J. Xiao, Y. Zhang, Z. Zhang, Q. Lv, F. Jing, K. Chi, S. Wang, *ACS Appl. Mater. Interfaces* **2017**, 9, 22604.
- [125] S. Chen, J. Duan, J. Ran, S. Qiao, *Adv. Sci.* **2015**, 2, 1400015.
- [126] C. Zhang, S. Bhoyate, M. Hyatt, B. L. Neria, K. Siam, P. Kahol, M. Ghimire, S. Mishra, F. Perez, R. K. Gupta, *Surf. Coat. Technol.* **2018**, 347, 407.
- [127] M. Wei, B. Li, C. Jin, Y. Ni, C. Li, X. Pan, J. Sun, C. Yang, R. Yang, *Energy Storage Mater.* **2019**, 17, 226.
- [128] G. Ren, Q. Chen, J. Zheng, B. Huang, Y. Qian, *J. Electroanal. Chem.* **2018**, 829, 177.
- [129] N. Cheng, Q. Liu, J. Tian, Y. Xue, A. M. Asiri, H. Jiang, Y. He, X. Sun, *Chem. Commun.* **2015**, 51, 1616.
- [130] Z. Liu, Z. Zhao, Y. Wang, S. Dou, D. Yan, D. Liu, Z. Xia, S. Wang, *Adv. Mater.* **2017**, 29, 1606207.
- [131] H. F. Wang, C. Tang, B. Wang, B. Q. Li, X. Cui, Q. Zhang, *Energy Storage Mater.* **2018**, 15, 124.
- [132] T. Y. Ma, J. Ran, S. Dai, M. Jaroniec, S. Z. Qiao, *Angew. Chem., Int. Ed.* **2015**, 54, 4646.
- [133] Y. Zhang, X. Xia, X. Cao, B. Zhang, N. H. Tiep, H. He, S. Chen, Y. Huang, H. J. Fan, *Adv. Energy Mater.* **2017**, 7, 1700220.
- [134] Z. Lu, W. Xu, J. Ma, Y. Li, X. Sun, L. Jiang, *Adv. Mater.* **2016**, 28, 7155.
- [135] Y. P. Zhu, Y. Jing, A. Vasileff, T. Heine, S. Z. Qiao, *Adv. Energy Mater.* **2017**, 7, 1602928.
- [136] M. Ma, F. Qu, X. Ji, D. Liu, S. Hao, G. Du, A. M. Asiri, Y. Yao, L. Chen, X. Sun, *Small* **2017**, 13, 1700394.
- [137] X. Ji, L. Cui, D. Liu, S. Hao, J. Liu, F. Qu, Y. Ma, G. Du, A. M. Asiri, X. Sun, *Chem. Commun.* **2017**, 53, 3070.
- [138] R. Zhang, Z. Wang, S. Hao, R. Ge, X. Ren, F. Qu, G. Du, A. M. Asiri, B. Zheng, X. Sun, *ACS Sustainable Chem. Eng.* **2017**, 5, 8518.
- [139] R. Ge, M. Ma, X. Ren, F. Qu, Z. Liu, G. Du, A. M. Asiri, L. Chen, B. Zheng, X. Sun, *Chem. Commun.* **2017**, 53, 7812.
- [140] Q. Liu, A. M. Asiri, X. Sun, *Electrochem. Commun.* **2014**, 49, 21.
- [141] R. Chen, H. Y. Wang, J. Miao, H. Yang, B. Liu, *Nano Energy* **2015**, 11, 333.
- [142] P. Chen, K. Xu, Z. Fang, Y. Tong, J. Wu, X. Lu, X. Peng, H. Ding, C. Wu, Y. Xie, *Angew. Chem., Int. Ed.* **2015**, 54, 14710.
- [143] M. S. Balogun, W. Qiu, H. Yang, W. Fan, Y. Huang, P. Fang, G. Li, H. Ji, Y. Tong, *Energy Environ. Sci.* **2016**, 9, 3411.
- [144] X. Wang, W. Li, D. Xiong, D. Y. Petrovykh, L. Liu, *Adv. Funct. Mater.* **2016**, 26, 4067.
- [145] X. Ma, X. Li, A. D. Jagadale, X. Hao, A. Abudula, G. Guan, *Int. J. Hydrogen Energy* **2016**, 41, 14553.
- [146] X. Li, X. Du, X. Ma, Z. Wang, X. Hao, A. Abudula, A. Yoshida, G. Guan, *Electrochim. Acta* **2017**, 250, 77.
- [147] G. Li, X. Wang, M. H. Seo, S. Hemmati, A. Yu, Z. Chen, *J. Mater. Chem. A* **2017**, 5, 10895.
- [148] J. Wang, X. Ma, F. Qu, A. M. Asiri, X. Sun, *Inorg. Chem.* **2017**, 56, 1041.
- [149] X. Wang, Y. Zheng, J. Yuan, J. Shen, J. Hu, A. Wang, L. Wu, L. Niu, *Electrochim. Acta* **2017**, 225, 503.
- [150] S. Hao, Y. Yang, *J. Mater. Chem. A* **2017**, 5, 12091.
- [151] K. Zhang, X. Xia, S. Deng, D. Xie, Y. Lu, Y. Wang, J. Wu, X. Wang, J. Tu, *J. Energy Chem.* **2019**, 37, 13.
- [152] N. Han, K. R. Yang, Z. Lu, Y. Li, W. Xu, T. Gao, Z. Cai, Y. Zhang, V. S. Batista, W. Liu, *Nat. Commun.* **2018**, 9, 924.
- [153] S. Cao, Z. Wu, B. Fu, H. Yu, L. Piao, *Catal. Today* **2019**, 330, 246.
- [154] J. Lai, S. Li, F. Wu, M. Saqib, R. Luque, G. Xu, *Energy Environ. Sci.* **2016**, 9, 1210.
- [155] Q. Dong, Q. Wang, Z. Dai, H. Qiu, X. Dong, *ACS Appl. Mater. Interfaces* **2016**, 8, 26902.
- [156] F. Meng, H. Zhong, D. Bao, J. Yan, X. Zhang, *J. Am. Chem. Soc.* **2016**, 138, 10226.
- [157] Y. Zhang, H. Sun, Y. Qiu, X. Ji, T. Ma, F. Gao, Z. Ma, B. Zhang, P. Hu, *Carbon* **2019**, 144, 370.
- [158] B. Zhang, E. Zhang, S. Wang, Y. Zhang, Z. Ma, Y. Qiu, *J. Colloid Interface Sci.* **2019**, 543, 84.
- [159] H. Liang, X. Cao, F. Zhou, C. Cui, W. Zhang, S. Yu, *Adv. Mater.* **2011**, 23, 1467.
- [160] Z. Wu, X. Xu, B. Hu, H. Liang, Y. Lin, L. Chen, S. Yu, *Angew. Chem., Int. Ed.* **2015**, 54, 8179.
- [161] T. Liu, Y. Liang, Q. Liu, X. Sun, Y. He, A. M. Asiri, *Electrochem. Commun.* **2015**, 60, 92.
- [162] S. Fu, C. Zhu, J. Song, M. H. Engelhard, X. Li, P. Zhang, H. Xia, D. Du, Y. Lin, *Nano Res.* **2017**, 10, 1888.
- [163] X. Ren, R. Ge, Y. Zhang, D. Liu, D. Wu, X. Sun, B. Du, Q. Wei, *J. Mater. Chem. A* **2017**, 5, 7291.
- [164] R. Ge, X. Ren, F. Qu, D. Liu, M. Ma, S. Hao, G. Du, A. M. Asiri, L. Chen, X. Sun, *Chem. – Eur. J.* **2017**, 23, 6959.
- [165] L. Yang, D. Liu, S. Hao, R. Kong, A. M. Asiri, C. Zhang, X. Sun, *J. Mater. Chem. A* **2017**, 5, 7305.
- [166] C. Xie, Y. Wang, D. Yan, L. Tao, S. Wang, *Nanoscale* **2017**, 9, 16059.
- [167] D. U. Lee, J. Choi, K. Feng, H. W. Park, Z. Chen, *Adv. Energy Mater.* **2014**, 4, 1301389.
- [168] J. S. Chen, J. Ren, M. Shalom, T. Fellingner, M. Antonietti, *ACS Appl. Mater. Interfaces* **2016**, 8, 5509.
- [169] G. Cai, W. Zhang, L. Jiao, S. Yu, H. Jiang, *Chem* **2017**, 2, 791.
- [170] Q. Zhang, H. Zhong, F. Meng, D. Bao, X. Zhang, X. Wei, *Nano Res.* **2018**, 11, 1294.
- [171] H. S. Jadhav, A. Roy, G. M. Thorat, W.-J. Chung, J. G. Seo, *J. Ind. Eng. Chem.* **2019**, 71, 452.
- [172] Z. Chen, C. X. Kronawitter, Y. W. Yeh, X. Yang, P. Zhao, N. Yao, B. E. Koel, *J. Mater. Chem. A* **2017**, 5, 842.